

Comparative petrophysical characterization, BIB-SEM imaging and permeability models of tight carbonates: Case study Upper Jurassic (Malm β), N Bavaria

Simon Freitag (✉ simon.s.freitag@fau.de)

Friedrich-Alexander-Universitaet Erlangen-Nuernberg <https://orcid.org/0000-0003-1972-0270>

Jop Klaver

MaP - Microstructure and Pores GmbH

Iulian S. Malai

Shearwater GeoServices

Norbert Klitzsch

RWTH Aachen University

Janos L. Urai

RWTH Aachen University

Harald Stollhofen

Friedrich-Alexander-Universitaet Erlangen-Nuernberg

Wolfgang Bauer

Friedrich-Alexander-Universitaet Erlangen-Nuernberg

Joyce Schmatz

MaP- Microstructure and Pores GmbH

Research

Keywords: Porosity, Permeability, Permeability models, Malm, Geomechanics

Posted Date: June 6th, 2022

DOI: <https://doi.org/10.21203/rs.3.rs-1679323/v1>

License:   This work is licensed under a Creative Commons Attribution 4.0 International License.

[Read Full License](#)

Comparative petrophysical characterization, BIB-SEM imaging and permeability models of tight carbonates: Case study Upper Jurassic (Malm β), N Bavaria

Simon Freitag¹, Jop Klaver^{2,5}, Iulian S. Malai^{2,3}, Norbert Klitzsch⁴, Janos L. Urai^{2,6}, Harald Stollhofen¹, Wolfgang Bauer¹, Joyce Schmatz^{2,5}

¹ GeoZentrum Nordbayern, Friedrich-Alexander-Universität (FAU) Erlangen-Nürnberg, Schlossgarten 5, 91054 Erlangen, Germany.

² RWTH Aachen University, Structural Geology, Tectonics and Geomechanics, Lochnerstrasse 4-20, 52064 Aachen, Germany.

³ now at: Shearwater GeoServices, 77 Mount Ephraim, Brockbourne House, Tunbridge Wells, Kent TN4 8BS, United Kingdom.

⁴ RWTH Aachen University, Applied Geophysics and Geothermal Energy (E.ON Energy Research Center), Mathieustraße 10, 52074 Aachen, Germany.

⁵ now at: MaP – Microstructure and Pores GmbH, Junkerstrasse 93, 52064 Aachen, Germany.

⁶ GeoStructures Consultancy for Structural geology and Geomechanics, Maastricht.

Correspondence should be addressed to Simon Freitag; simon.s.freitag@fau.de

Keywords: Porosity, Permeability, Permeability models, Malm, Geomechanics

Abstract

Tight carbonate rocks are important potential although unconventional geothermal and hydrocarbon underground storage reservoirs and prospective CO₂-EGS sites. We study these rocks by using the Upper Jurassic “Malm β” in Southern Germany as an outcrop analog example to understand bulk properties in relation to microstructure and to test a variety of models for permeability prediction. Bulk petrophysical methods (Archimedes isopropanol immersion method, Helium pycnometry, mercury

injection capillary pressure, gamma density core logging, gas permeability measurements) combined with microstructural investigations (BIB-SEM) are applied. Samples are macroscopically undeformed limestones collected from a tectonically overprinted quarry wall near the town of Simmelsdorf (38 km NE of Nürnberg city). Bulk porosities are below 5% and argon permeabilities are on average $1.4\text{E-}17\text{m}^2$. The presence of stylolites in some of the samples has neither a significant effect on porosity nor permeability. Pore sizes are in the submicron range and the diagenetically lithified stiff limestones are characterized by a relatively high Young's Modulus averaging 73 ± 5 MPa. Moreover, no trends in properties were observable towards the faults, indicating that faulting was post-diagenetic and that the matrix permeabilities were too low for intensive post-diagenetic fluid-rock interaction. Petrophysical properties are very close to those measured in stratigraphic equivalent rocks of the South German Molasse Basin, illustrating the widespread homogeneity of these rocks and justifying the quarry scale (500 x 580 m) as a reasonable reservoir analog for these rocks in the subsurface. The application of various permeability prediction models showed that the Capillary Tube model and the Saki Model are very well suited for predicting permeabilities from BIB-SEM and mercury injection capillary pressure results, respectively. We thereby found that the matrix permeability is primarily controlled by the pore throat diameters rather than the effective porosity.

1. Introduction

The desired energy transition towards carbon-neutral non-fossil energy sources requires consideration of not only conventional but also of yet underexplored unconventional regenerative energy sources such as Enhanced Geothermal Systems (EGS). Geothermal power plants producing from tight but high thermal conductivity carbonate rocks bear the potential of playing a vital role in the energy transition (e.g. Gosnold et al., 2010; Hofmann et al., 2014). Such reservoirs are characterized by very low matrix permeabilities, typically in the range of 0.001-10 mD (Akanji et al., 2013), implying that fluid transport in tight carbonate rocks is mostly focused to fractures and faults (Al-Obaid et al., 2005; Dimmen et al., 2017; Litsey et al., 1986; O'Neill, 1988; Zeybeck and Kuchuk, 2002) with only minor fluid flow through the rock matrix (Bohnsack et al., 2020). Moreover, microporosity and -structures may impact fracture

pattern, fracture density, fracture propagation behavior and thus effectivity of carbonate matrix stimulation treatments (Barri et al., 2021; Ziaudin & Bize, 2007).

A major geothermal aquifer in southern Germany is the Upper Jurassic (Malm) limestone reservoir actually tapped by >22 geothermal power plants in the South German Molasse Basin. As geophysical borehole measurements or cores from this tight aquifer are scarce, incomplete, or often even non-existent (Bohnsack et al., 2020), petrophysical investigations on rock samples from reservoir analogs of equivalent stratigraphic units are common practice. The tight carbonates of the Upper Jurassic Malm β carbonates, for instance, are part of the geothermal aquifer in the South German Molasse Basin (SGMB), although not the primary target. These units represent an excellent opportunity to compare petrophysical investigation of deeply buried rocks (1-3 km) to those of the same stratigraphic units exposed on the Franconian Alb located about 200 km to the north of the geothermal target lithology in the SGMB where maximum burial of c. 1100 m has been recently quantified (Freitag et al. in review). In terms of lithofacies, the Malm β carbonates in South Germany can be classified predominantly as mud- to wackestones (Koch and Weiss, 2005).

The main goal of this study is to characterize the investigated rocks in terms of their petrophysical and microstructural properties, their lateral and vertical variability, and the structural anisotropy of exemplarily chosen tight carbonates. Acquired data aim to assess their heterogeneity and to better estimate the contribution of fluid transport from the matrix to the fracture system at field scale for modeling purposes. As, for instance Haines et al. (2016) proposed that the pore system in tight carbonates is primarily controlled by their lithofacies and then modified by diagenetic and tectonic processes also the petrophysical properties and pore characteristics of the matrix across carbonate rock-hosted normal fault zones will be assessed. We further investigate the hydraulic influence of stylolites, which can form either barriers (Rashid et al., 2017) or conduits for fluid flow (Bruna et al., 2019), as they are typically responsible for most of the variability in petrophysical properties in these rock types. We then evaluate the stiffness of the rock and discuss, whether the petrophysical properties of the investigated uplifted rocks are applicable to buried reservoir rocks of the same stratigraphic units in the Molasse Basin, where Bohnsack et al. (2020) conducted an extensive study with a similar focus, but

with a different approach. Similar studies have been conducted by Beichel et al. (2014), Böhm et al. (2010), and Hedtmann and Alber (2017), however, none of these studies did include samples of the Malm β carbonates, hence an objective comparison of results is not possible. Further studies on the petrophysical reservoir rock properties of the Malm β have only been conducted on exposed outcrop analogs of the Upper Jurassic target formation (Malm β) in the South German Molasse Basin by Mraz et al. (2018) and Homuth et al. (2014, 2015), which will be used for comparison with our results.

A second aim is more technical. As for many geothermal reservoirs only limited sample volumes are available, petrophysical data of the target rock formation determined from cuttings are essential for subsequent reservoir quality evaluation and modeling. These cuttings are investigated by mercury intrusion capillary pressure (MICP) measurements and broad ion beam scanning electron microscopy (BIB-SEM). Based on MICP measurements, bulk information on quantitative pore characteristics, including the pore throat size distribution can be obtained, down to a pore throat size of only 3 nm (Clarkson et al., 2013; Giesche, 2006; Okolo et al., 2015; Webb, 2001; Xu et al., 2018; Zhao et al., 2018). Also, based on MICP data permeability estimations through a variety of permeability estimation models are possible. Therefore, this method is considered as a standard for the investigation of tight reservoir rocks (Gao et al., 2016; Okolo et al., 2015). We evaluate various existing permeability models, mainly based on MICP measurements, by comparing them to steady-state Darcy flow/permeability measurements. The BIB-SEM application enables microstructural investigation of relatively small rock pieces and quantification of pore sizes down to c. 5 nm (Klaver et al., 2012). Additional capillary tube modeling then provides a solid basis for comparison with permeability measurements in tight rocks (Philipp et al., 2017; Sinn et al., 2017).

2. Geological background

During the Jurassic, the study area was situated in an epicontinental sea as part of the northern to northwestern Tethys shelf (e.g. Koch and Weiss, 2005; Meyer, 1996; Pieńkowski et al., 2008). Stress-induced lithospheric deflections related to far-field compression (Scheck-Wenderoth et al., 2008) and a wrench-dominated tectonic regime at the southern end of the North Sea rift system (Pharaoh et al., 2010) during the latest Jurassic to earliest Cretaceous led to rapid shallowing of the South German shelf areas,

resulting in the deposition of peritidal carbonates and anhydrites, and ultimately to their exposure and pronounced erosion (Bachmann et al., 1987; Schröder, 1968; Vejbæk et al., 2010; Voigt et al., 2007, 2008; Ziegler, 1990). Widespread post-Jurassic, Mid- to Late-Cretaceous erosion and karstification was followed by a sea-level rise, recorded by a northward marine transgression (Bachmann et al., 1987, Scheck-Wenderoth et al., 2008). After a phase of tectonic quiescence, N-S to NW-SE oriented far-field compressive stresses within the Central European lithosphere related to the Alpine Orogeny (e.g. Scheck-Wenderoth et al., 2008, Ziegler, 1987; Ziegler et al., 1995) or the onset of Africa-Iberia-Europe convergence (Kley and Voigt, 2008) caused the Late Cretaceous inversion. Ultimately, the Late Cretaceous inversion not only led to the cessation of Cretaceous sedimentation but also to the erosion of several hundreds of meters of Mesozoic sediments and the reverse reactivation of faults (Bachmann et al., 1987; von Eynatten et al., 2021; Fazlikhani et al., 2022; Scheck-Wenderoth et al., 2008; Voigt et al., 2008, 2021). A second major uplift phase followed between the latest Late Cretaceous and Palaeocene caused by the Alpine continental collision (Peterek et al., 1997; Reicherter et al., 2008; Schröder, 1987; Wagner et al., 1997; Ziegler, 1987) and by mantle-induced domal uplift below the Upper Rhine Graben Rift to the west of the study area (von Eynatten et al., 2021). Significant Cretaceous and Cenozoic sediments are only preserved within the South German Molasse Basin further to the south of the study area (Bachmann and Müller, 1992; Meyer, 1996).

The investigated limestones, classified as mud- to wackestones, were deposited during the Oxfordian to Lower Kimmeridgian (163.5 – 157.3 Ma)(Cohen et al., 2013; Koch and Weiss, 2005). Massive limestones of the “Hartmannshof formation” containing abundant siliceous sponges represent a reefal facies (Pińkowski et al., 2008) following basal marls that are overlying the “Ornatenton” (Dogger) (Zeiss, 1977). As the “Hartmannshof” formation contains large amounts of ammonites, belemnites, and brachiopods, a semi-pelagic depositional environment at intermediate water depths characterized by marl deposition and numerous siliceous sponge reefs is inferred by Pińkowski et al. (2008) and Zeiss (1977). Thick marl beds of the Malm γ mark the top of the “Hartmannshof” formation and its stratigraphic boundary to the overlying “Arzberg” formation (Lower Kimmeridgian) (Koch and Weiss, 2005; Meyer, 1974; Zeiss, 1977).

The tectonic processes during the late Jurassic – early Cretaceous, which led to the reactivation of NW-SE and NNE-SSW striking faults, are recorded by small offsets (≤ 2 m), of NW-WE striking normal faults in the examined quarry. Subsequent transpressional forces associated with the Alpine Orogeny resulted in the formation of N-S trending strike-slip faults (offset only a few centimeters) as well as the reversed reactivation of NW-SE striking normal faults, both present in the quarry. At a smaller scale, stylolites are prominent, mostly on vertically oriented planes, bedding parallel and sub-parallel to the strike of normal faults (Köhler et al., in review).

3. Materials and Methods

3.1. Sampling

The investigated test field is located in an active quarry near the town of Simmelsdorf, about 38 km to the northeast of Nuremberg (Figure 1a), exposing Upper Jurassic (Malm) limestones in the south-eastern extension of the South German scarpland. A total of 40 carbonate samples were collected for this study from a NNE-SSW outcrop section (Figure 1b), which is oriented perpendicular to a set of conjugate normal faults. The offset of the normal faults is relatively small, approximately 0.5 m with sub-horizontal beds varying in thickness from 0.1 – 0.6 m (see Figure 1). Blocks (~ 50 cm x 50 cm x 40 cm) of each bed (B-1 to B10) were systematically sampled in a vertical section, approximately one meter distant from the fault. For a horizontal section, blocks of similar size were extracted from bed B1 every few meters (see also Figure 1b for the approximate locations). The blocks were carefully removed by an excavator, layer by layer. They were cut on-site into smaller pieces and a selection of samples from the vertical section was drilled with c. 6 cm and 3 cm diameters to get cores and plugs suitable for the Multi-Sensor Core Logger (MSCL-S), gas permeability (plugs), and helium porosimetry (plugs), and the BIB-SEM analyses (sub-samples of plug ends). Cores were always drilled from the non-fractured part of the blocks and sedimentological section measurements were carried out as a preliminary analysis to identify local lithological heterogeneities and to provide guidance on where to subsample the cylinder-shaped plugs (3 x 4 cm) for the petrophysical measurements and further BIB-SEM investigations. The presence and orientation of stylolites was noted for each plug. Additional 40 plugs and sub-samples were taken from all pieces of both, the vertical as well as the horizontal sections for gas permeability

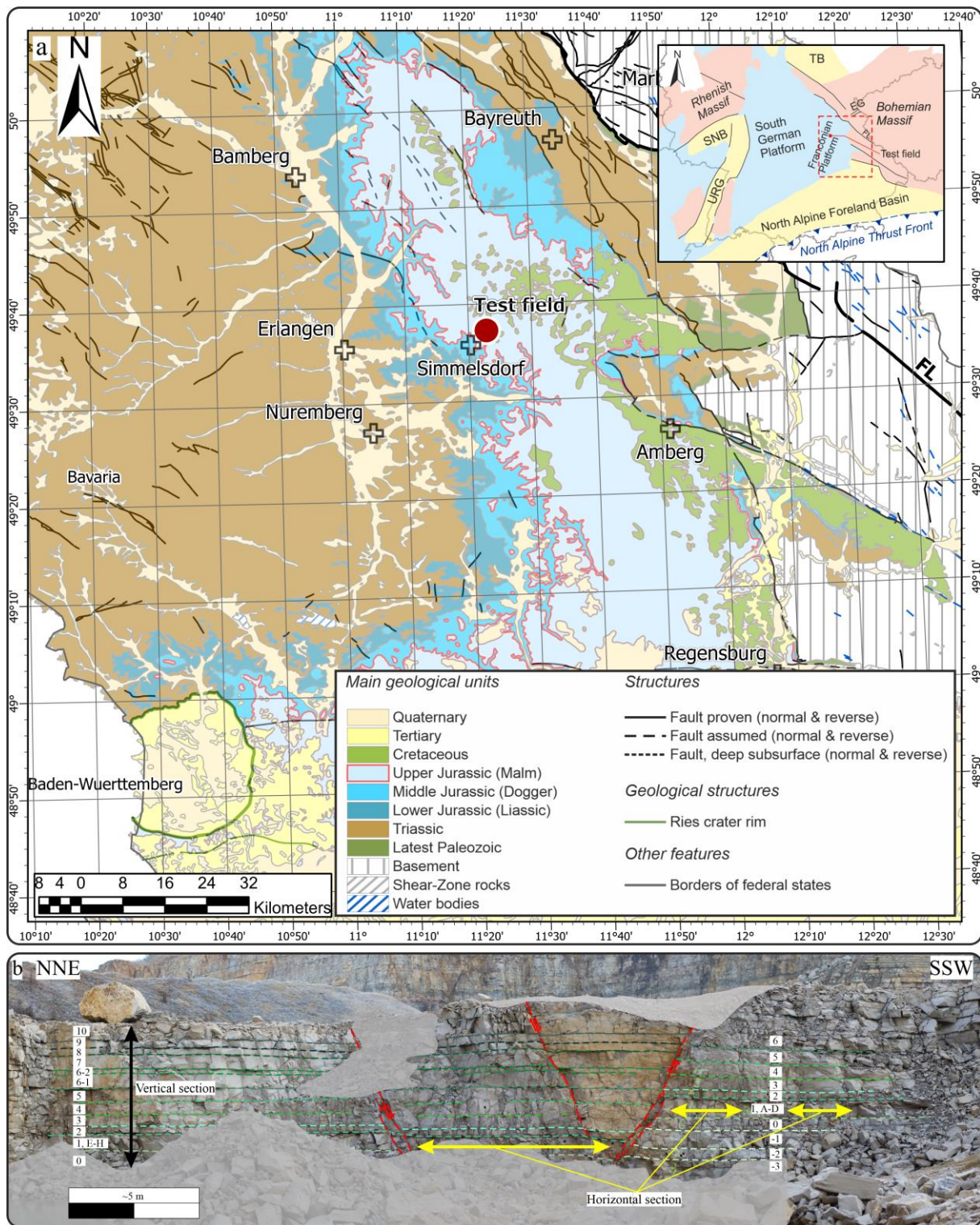


Figure 1: Geological map of northern Bavaria, showing major stratigraphic units, structural features, and the test field location ~30 km NE of Nuremberg. Background data source: Bayerisches Landesamt für Umwelt, www.lfu.bayern.de. The city-data (transparent crosses) were provided by MapCruzin.com (downloaded: 19 July 2021 at 9:45). The administrative region data belong to © GeoBasis-DE / BKG (2021). **b)** Photograph of the sampled rock section at Simmelsdorf quarry (see red dot in Fig. 1a for location), with structural features and sediment bed numbers labeled.

(plugs) and supplementary MICP measurements (sub-samples). All plug samples were dried in an oven at 105°C until weight constancy was reached over a period of 24 hours before any kind of analysis were performed.

3.2. BIB-SEM

The plug ends of each selected bed sample from the vertical section were sub-sampled for microstructural analyses using BIB-SEM. The 5 sub-samples have maximum dimensions of 4 x 10 x 6 mm³ (height x width x depth) and were taken from a macroscale relatively homogenous, representative part of the plug ends. The BIB cross-section was polished using the JEOL SM-09010 cross-section polisher producing a 1 mm² planar Gaussian-shaped cross-section on the sample by removing approximately 100 µm of material in 8 hours (Klaver et al., 2012). Prior to SEM image mapping by a Zeiss Supra 55 Field Emission SEM, samples were prepared with approximately 7.5 nm of tungsten coating. In the SEM, the pore space was imaged with the secondary electron (SE2) detector systematically in a raster pattern throughout the whole BIB section at about 50 locations without overlap. At each location 5 images were acquired with different magnifications of 2,500, 5,000, 10,000, 20,000, and 40,000 times. This approach enables unbiased sampling of the whole section and scans a wide range of pore sizes simultaneously. The visible BIB-SEM porosity was quantified by calculating the fraction of visible pore space using image segmentation (Klaver et al., 2012) for 5 selected cross-sections on several single images. The other BIB cross-sections were used for qualitative investigations as the pore microstructures were similar to each other from visual inspection.

Two additional sub-samples were injected with Wood's Metal (LMI-BIB-SEM) according to Klaver et al. (2015) at 100 and 200 MPa, respectively. As Wood's Metal has non-wetting properties comparable to mercury, it is a similar principle as MICP, though the Wood's Metal is solid at room temperature, which enables visualizing the metal-filled pore space. Subsequently, after BIB low angle polishing in a Leica TIC3X BIB, the metal-filled pore space was imaged in the SEM to qualitatively evaluate the pore connectivity in the carbonate matrix.

3.3 Petrophysical Methods

In this section, first all petrophysical methods for measuring the effective porosity, the multi-sensor core logger (MSCL), the Archimedes isopropanol immersion method, the Helium pycnometry, the Wood's Metal injection, the Mercury injection capillary pressure method (MICP), and the BIB-SEM method are shortly described. Latter three methods also give insight into the pore throat size and pore size distribution for pores larger 3 nm. Thereafter, the derivation of geomechanical rock properties is explained. Complementary permeability measurement methods, as well as various models for permeability estimations using different MICP- and BIB-SEM-derived parameters, are finally described.

3.3.1. Multi-Sensor Core Logger (MSCL)

The Geotek Multi-Sensor Core Logger (MSCL) system includes an assembly of tools that log the geophysical and geochemical properties of cores (diameter 5-15 cm). A heavy-duty core pusher guides the cores along the sensors at a precision of 0.01 mm. For this study, only the gamma density tool was used, which consists of a gamma-ray source and detector mounted across the core. A total of 0.94 m core lengths was measured. The samples were subjected to a focussed beam of gamma rays (energies principally at 0.662 MeV) that become attenuated by Compton scattering while they pass through the core with the degree of attenuation directly relating to the diameter and the electron density of the core. The bulk density (ρ_{bulk}) of the measured core section was then calculated by measuring the number of transmitted gamma photons that passed through the core unattenuated (I), considering the core thickness (d):

$$\rho_{bulk} = \frac{1}{\mu d} \ln \frac{I_0}{I} \quad (1)$$

where μ is the Compton attenuation coefficient and I_0 the gamma source intensity. The porosity Φ , in the following termed gamma ray (GR) porosity is calculated applying bulk density (ρ_{bulk}), matrix density ($\rho_{matrix} = 2.71 \text{ g/cm}^3$ for CaCO_3), and the density of air ($\rho_{air} = 0.001225 \text{ g/cm}^3$):

$$\Phi = \frac{\rho_{matrix} - \rho_{bulk}}{\rho_{matrix} - \rho_{air}} \quad (2)$$

3.3.2. Archimedes (buoyancy) isopropanol immersion method

The Archimedes method is a simple and direct method to measure the effective porosity by using the principle of buoyancy and was applied to a total of 40 drilled cylindric core plugs. Advantages, disadvantages, operating principle, and potential measurement errors of the method are thoroughly discussed by Hall and Hamilton (2016). The Archimedes porosity Φ (%) was calculated via Equation 3:

$$\Phi = \frac{V_P}{V_{tot}} = \frac{m_{sat} - m_{dry}}{m_{sat} - m_{im}} \quad (3)$$

where V_P (m³) is the open pore space volume filled with isopropanol, derived from subtracting the dry mass m_{dry} (g) from the saturated mass m_{sat} (g). V_{tot} (m³) is the total volume of the sample including the open pore space and the solid rock matrix volume, which is equal to the difference between the saturated mass m_{sat} and the weight m_{im} (g) of the sample submerged in isopropanol. The weights were determined using the Sartorius ED2245 with an accuracy of 0.1 mg. Only the open pores that are connected to the open pore network of the sample can be determined, as the isopropanol cannot access closed pores (Zinszner and Pellerin, 2007).

3.3.3. He-pycnometry

Helium porosity measurements were carried out on 40 selected plugs from the horizontal and vertical sections. The porosities were calculated based on the difference between the total dry plug volume (calculated from diameter and length measures by a high precision gauge) and the matrix volumes determined by a Micromeritics AccuPyc 1330 pycnometer. The instrument measures the skeletal volume of a sample with an accuracy of 0.03% (i.e. matrix volume) by the gas displacement technique based on the ideal gas law with the application of helium enabling the filling of pores connected to the open pore network as small as 0.1 nm in diameter.

3.2.5. Mercury injection capillary pressure (MICP)

Mercury intrusion porosimetry is one of the most widely used methods to determine the total porosity and the pore (throat) size distribution by utilizing the property of non-wetting liquids that only intrude

capillaries under pressure. Washburn (1921) described this relationship between pressure and capillary diameter:

$$P = \frac{-4\gamma \cos \theta}{d} \quad (4)$$

where P = pressure, γ = surface tension of the liquid (in this case mercury), θ = contact angle of the liquid (for mercury $\theta = 140^\circ$), and d = diameter of the capillary. The intruded volume of mercury entering the pores at each pressure increment is recorded and from that, the pore (throat) size distribution is derived, whereas the total porosity can be calculated from the total intruded mercury volume (Abell et al., 1999). The R_{35} values correspond to the pore diameter at 35% mercury saturation while R_{Main} gives the pore diameter where the largest amount of mercury intruded, both listed in Table 1. We used the PoreMaster 60 by Quantachrome with an accuracy of $\pm 1\%$ fso (full Scale Output) of sample cell stem volume on 24 samples.

3.3.4. Geomechanical properties

Geomechanical parameters such as the Poisson's number ν , dynamic Young's Modulus E (GPa), and the Bulk Modulus K (GPa) are calculated from P- (V_P) and S-wave (V_S) velocities (m/s) which were measured on 33 limestone samples by using the MSCL. Only plugs that were drilled vertically to bedding were measured. For a detailed description of the operating principle of the MSCL see the study of Filomena and Stollhofen (2011). The Poisson's number ν was derived from the following equation

$$\nu = (0.5 * V_P^2 - V_S^2) * (V_P^2 + V_S^2)^{-1}. \quad (5)$$

The Young's Modulus E is calculated:

$$E = ((1 + \nu) * (1 - 2\nu) / (1 - \nu)) * V_P^2 * m_{dry} / V_{Ges}, \quad (6)$$

where m_{dry} and V_{Ges} were determined by the Archimedes method. The Bulk Modulus K is then based on the following equation (Berryman, 1992):

$$K = E / (3 - 6 * \nu) = -dp/dV/V > 0. \quad (7)$$

3.3.5. Permeability measurements

Gas permeability measurements (in m^2) were carried out using argon on 12 samples. The 1-inch diameter plugs were placed inside a stainless-steel cylinder (Autoclave) and permeability determinations were carried out at increasing gas pressure steps of 1 bar with a confining pressure P_{conf} of 15 bar. For each plug, the flow rate through the sample was measured at six different pressure steps P_{inj} , from 3 to 8 bar to correct for the so-called “Klinkenberg Effect”, see Klinkenberg (1941) for more details. After each pressure increment, the flow was measured once measurements were stable for at least ten minutes before proceeding to the next step.

A similar method was applied to determine the permeability of all samples (34), however, using compressed air instead of argon (in m^2). When a stable flow after a minimum of 10 minutes was established at each pressure increment, the gas (air) flow rate leaving the sample was measured every second over a period of 30 seconds. An “Aarberg” mass flow meter with an accuracy of 1% at flow rates between 0 to 50 ml/min was used as logging device. Due to mechanical limitations, a confining pressure of only 8 bar could be applied. Therefore, the maximum flow rate through the sample was reached at a pressure of 5.8 bar, before the through-flowing air might have bypassed the sample due to a too low difference between confining and injection pressure. A Klinkenberg correction for the permeability measurements with air was not possible, as we received negative slippage factors. Possible reasons for that are discussed later. We, therefore, used the uncorrected, mean measured permeabilities for the comparison to other applied methods and models.

3.4. Permeability models

Many different permeability models that were calibrated or validated on different sample sets over the last decades were applied to our data set but only the permeability estimation models that performed best will be treated and discussed in this study.

3.4.1. Models based on percolation theory

Permeability estimation based on MICP was introduced by Katz and Thompson (1986, 1987). Their model is based on the percolation theory (K-T Model) and relates the pore diameter l (m) to the intrinsic permeability k_{KT} (m²). When l is optimally selected, k_{KT} (m²) can be derived via Equation 8

$$k_{KT} = \frac{1}{89} \Phi \frac{(l_{max}^h)^3}{l_c} f(l_{max}^h) \quad (8)$$

where ϕ represents the porosity of the rock, l_c (m) the critical length, l_{max}^h (m) the maximum hydraulic length and the fraction of the whole rock $f(l_{max}^h)$ that is filled by mercury at l_{max}^h . While critical length l_c is defined as the critical pore diameter at which mercury can finally percolate through the sample (equal to the steepest slope of the capillary pressure vs. cumulative porosity curve after cut-off), l_{max}^h corresponds to the capillary pressure, where the product of the mercury saturation and the cubic pore throat diameter, $f(l_{max}^h) * l^3$, is maximum (Nishiyama and Yokoyama, 2014; Rashid et al., 2015). Originally, the theoretical consideration that the pore's diameter is equal to its length led to the constant 1/89 (Nishiyama and Yokoyama, 2014; Rashid et al., 2015). However, this constant was empirically determined for porous rocks. As this study focuses entirely on tight carbonates, a value of 1013/89 for C was used instead, based on the work of Rashid et al. (2015) who recommends this value for tight carbonates.

3.4.2. Poiseuille-based models

Rashid et al. (2015) apply eight permeability models which are based on the Poiseuille model. We tested a selection of these models, too. The Winland model was originally introduced in various unpublished reports between 1972 and 1976, which we could not obtain; we therefore reference published studies by Comisky et al. (2007), Gunter et al. (2014), and Rashid et al. (2015). The Winland model uses the radius R_{35} [μm], which is calculated using the Washburn equation (Equation 4) at a mercury saturation of 35% (Rashid et al., 2017) and relates it to permeability k_w (in m²) according to:

$$k_w = C_w * R_{35}^{a_1} * \Phi^{a_2} * cf \quad (9)$$

where C_w , a_1 , and a_2 are empirically determined variables, Φ is the porosity, and cf ($= 9.86923 \times 10^{-16}$) the factor for converting milliDarcy [mD] to m^2 . These variables were derived from the calibration of Winland's equation on a dataset consisting of 82 samples, 56 of which were sandstones and 26 carbonates, for which the Klinkenberg-corrected permeabilities, as well as 240 samples, where only uncorrected air permeabilities were known. The calibration resulted in the following values: $C = 49.4$, $a_1 = 1.70$ and $a_2 = 1.47$.

Dastidar et al. (2007) introduced another Poiseuille-based permeability model (Dastidar Model), calibrated on tight gas sandstones. The authors suggest taking the entire pore throat spectrum into account when estimating the permeability from MICP-data. They introduce a length scale based on the geometric mean of the pore throat radius (R_{wgm}) which is calculated:

$$R_{wgm} = \left[\prod_{i=1}^n R_i^{w_i} \right]^{\frac{1}{\sum_{i=1}^n w_i}} \quad (10)$$

with the pore throat radius R_i at the i^{th} capillary pressure, the total number of incremental pressure steps n , and w_i the ratio of the incremental mercury volume intruded into the sample at the specific capillary pressure p_i and the total mercury volume intruded. With this, we can calculate permeability k_D (in m^2) after Dastidar et al. (2007), where cf is the factor for converting mD to m^2 :

$$k_D = 4073 * R_{wgm}^{1.64} * \Phi^{3.06} * cf \quad (11)$$

An alternative Poiseuille-based model is the capillary tube model that can be directly applied to the pore geometries determined from segmented BIB-SEM images. It assumes that the flow through the rock is analog to laminar flow through a bundle of pipes. As pore networks in rocks are never perfectly straight round tubes, but follow a tortuous path, a modified version of the Hagen-Poiseuille equation, taking into account the tortuosity factor τ (Philipp et al., 2017; Sinn et al., 2017), is employed to determine permeability k_{H-P} (in m^2) according to the Capillary Tube Model:

$$k_{H-P} = \frac{1}{8} \sum_{i=1}^n \frac{r_i^2 \Phi_i}{\tau^2} * cf \quad (12)$$

where r_i equals the hydraulic radius (pore area divided by its perimeter), Φ_i the porosity of each segmented pore in the BIB-SEM image, and cf the factor for converting mD to m². The tortuosity value can be a fitting parameter or taken from literature data. For this study, a tortuosity of 2.0 was assumed initially, as tight carbonates are slightly less tortuous than tight sandstones (Cai et al., 2019) with typical values of 2.1 (Du, 2019).

The Kozeny-Carman model (K-C Model) is an extension by Carman (1937) that bases on the permeability model developed by Kozeny (1927). He used the specific surface area related to the rock volume S_0 and the effective porosity Φ_{eff} , hence the pore space contributing to fluid flow (Fens, 2000):

$$k_{K-C} = c\tau^2 \frac{\Phi_{eff}^3}{S_0^2(1-\Phi_{eff})^2} * cf, \quad (13)$$

with the Kozeny constant c and τ as the tortuosity factor, the permeability k_{K-C} (in m²), based on the K-C Model), and cf the factor for converting mD to m². S_0 was obtained from MICP-data. The tortuosity factor τ is derived from the optimized capillary tube model and the Kozeny constant c for cylindrical capillaries is 2 (Carman, 1937).

3.4.3. Empirical models

Various empirical equations have been introduced, too. In this study, however, we only applied the models developed by Bohnsack et al. (2020), Saki et al. (2020), Lucia (2001), and Jennings and Lucia (2003).

Based on the porosity-permeability relationship measured on a subset of ~50 mud-supported limestones out of a set of 363 Upper Jurassic limestone core samples, Bohnsack et al. (2020) inferred the following power law (termed Bohnsack Model)

$$k_B = 2.0E^{-04} * \Phi^{3.10} * cf, \quad (14)$$

where k_B is the permeability (m²), Φ the effective water porosity (%), and cf the factor for converting mD to m².

Saki et al. (2020), on the other hand, established the following relationship (termed Saki Model) between gas permeability, porosity, and pore/throat diameters from 187 sandstone, limestone, and dolostone samples from 8 different Iranian oil and gas fields:

$$k_S = \exp(0.0583 + 1.4660 * \log r_{35} + 0.6993 * \log \Phi) * cf, \quad (15)$$

where k_S is the gas permeability (m²), Φ the porosity, R_{35} is the smallest pore throat radius (μm) filled by mercury at 35% mercury saturation, and cf the factor for converting mD to m².

An extensive study on a variety of limestones (n = 416) was conducted by Lucia (2001) and Jennings and Lucia (2003). They related rock-fabric petrophysical classes and interparticle porosity to permeability via a multilinear regression, termed global porosity-permeability transform (GPPT). Each rock-fabric petrophysical class represents a different type of pore distribution and interconnection (Lucia, 1995). Three classes are thereby distinguished and assigned a specific *rock fabric number* (rfn) (0.5-4.0): class 1 represents grainstones and coarsely crystalline dolostones with a rfn of 0.5 – 1.5, class 2 includes grain-supported packstones and medium crystalline dolostones with a rfn between 1.5 and 2.5, and class 3 comprises mud-supported limestones and fine crystalline dolostones with a rfn of 3.5 – 4.0 (Lucia, 2001). The global porosity-permeability transform (GPPT Model) is given by:

$$k_{GPPT} = \exp((A - B * \log(rfn)) + (C - D * \log(rfn)) * \log(\Phi_{ip})) * cf, \quad (16)$$

where k_{GPPT} is the rock permeability (in m²) based on Lucia (2001) and Jennings and Lucia (2003), A = 9.7982, B = 12.0838, C = 8.6711, D = 8.2965, Φ_{ip} the fractional interparticle porosity (effective porosity), and cf the factor for converting mD to m².

4. Results

Table 1: Summary of measured porosity and permeability values as well as various pore throat diameters that are used further on of all Simmelsdorf quarry Malm B samples (n = 40). See Figure 1 for sample positions.

Bed	Horizontal	Bed thickness	Distance from fault	Plug label*	Arch.-Porosity	GR-Porosity	He-Porosity	MICP	R _{Main}	R ₃₅	BIB-SEM porosity @ 20kx	Ar-Permeability K _{ar}	Air-Permeability K _{air}
-----	------------	---------------	---------------------	-------------	----------------	-------------	-------------	------	-------------------	-----------------	-------------------------	---------------------------------	-----------------------------------

[#]	[-]	[cm]	[m]	[-]	[%]	[%]	[%]	[%]	[nm]	[nm]	[%]	[m ²]	[m ²]
10		55	-	B10_NS	3.54		4.57	4.11	20.58	14.15			6.39 E-18
				C91H	2.86	5.58	5.77					1.51E-17	
				C91V	3.09	5.15	5.11				3.47	1.24E-17	9.02E-18
9		22	-	C92H	3.06	5.31	5.36	4.18	14.13	10.56		1.20E-17	9.09E-18
				B9_NS	3.79		5.45	2.03	10.68	7.72			7.82E-18
				B9_2_NS	3.11		3.17						
				C8H	1.98	3.68	4.05	3.54	4.93	4.45	2.46	1.37E-17	3.11E-18
				C8V	3.10	4.50	3.94					1.27E-17	
8		20	-	B8_NS	2.79		3.54	2.56	3.72	6.59			9.97E-18
				B8_EW	2.70		2.86						5.51E-18
				B8_V	3.38		3.87						5.50E-18
7		40	-	B7_NS	3.32		3.95	2.35	10.22	8.38			1.08E-17
				C62V	3.17	5.55	5.71	3.97	21.74	9.51		1.22E-17	5.27E-18
6.2		15	-	C62H2	1.12	5.11	5.32				3.52	2.10E-17	1.94E-18
				C62H1	3.33	5.89	6.05					1.19E-17	4.10E-18
				C61V	1.66	3.66	3.95				2.75	1.23E-17	
6.1		35	-	C61H2	1.75	4.11	4.23	4.39	14.68	9.15		1.41E-17	8.14E-18
				B6_NS	3.92		5.48	3.35	22.77	13.11			8.60E-18
				C5H2	2.86	5.32	5.00	4.08	21.56	12.93	2.12	1.58E-17	7.27E-18
				C5V	3.48	5.65	5.45					1.32E-17	6.32E-18
5		40	-	B5_NS	4.01		4.44	2.98	18.46	12.01			6.77E-18
				B5_V	4.18		4.80						7.62E-18
				B4_NS	3.95		4.62	3.42	23.61	12.75			1.08E-17
4		35	-	B4_2_NS	3.59		5.97						
3		32	-	B3_EW	3.53		3.91	2.98	18.92	11.78			3.49E-18
2		18	-	B2_NS	3.81		5.38	4.31	17.46	11.33			6.25E-18
1	D	45	6.0	B1D_NS	2.78		3.74	2.08	10.46	7.56			8.72E-18
1	C	45	4.5	B1C_NS	2.72		2.98	1.82	7.16	6.65			7.92E-18
1	B2	45	3.5	B1B_2_NS	3.23		4.47						
1	B1	45	2.0	B1B_1_NS	3.15		3.33	2.14	9.23	7.45			4.64E-18
1	A	45	0.5	B1A_NS	2.02		2.48	2.68	6.07	6.07			6.67E-18
1	F	45	-3.5	B1F_NS	2.29		3.56	3.39	13.90	9.31			5.89E-18
1	E	45	-5.0	B1E_NS	3.10		3.76	1.76	7.22	6.47			4.98E-18
1	G	45	-6.5	B1G_NS	1.43		2.80	1.94	7.51	6.43			4.61E-18
1	H	45	-8.5	B1H_NS	3.81		4.44	2.33	10.00	7.76			7.63E-18
				B1_NS	2.78		3.45	1.97	6.87	6.58			4.21E-18
1		45	-	B1_EW	2.88		3.15						6.10E-18
				B1_V	3.26		4.07						1.01E-17
0		30	-	B0_V	2.61		3.33	1.89	9.76	7.86			1.06E-17
-1		43	-	B-1_NS	4.10		5.21						8.41E-18
Number of measurements					40	12	40	24	24	24	5	12	34

*The plugs with bold labels contain clear stylolites at macroscale. The plug label extensions NS, EW, or V refer to the orientation of the plugs.

4.1. Microstructure and pore geometry

All plugs prepared for the gas (Ar) permeability tests were macroscopically investigated regarding presence and orientation of stylolites (Table 1*). Half of the plugs contained stylolites identifiable at macroscale, both sub-parallel to the bedding (Figure 2a) as well as sub-perpendicular to bedding (Figure 2b). Such pervasive stylolites were clearly visible in the SEM and were examined at very high detail in the BIB cross-section to determine and characterize different types of microporosity (pores < 1 micron) and nanoporosity (pores < 100 nm) (Figure 2c-f).

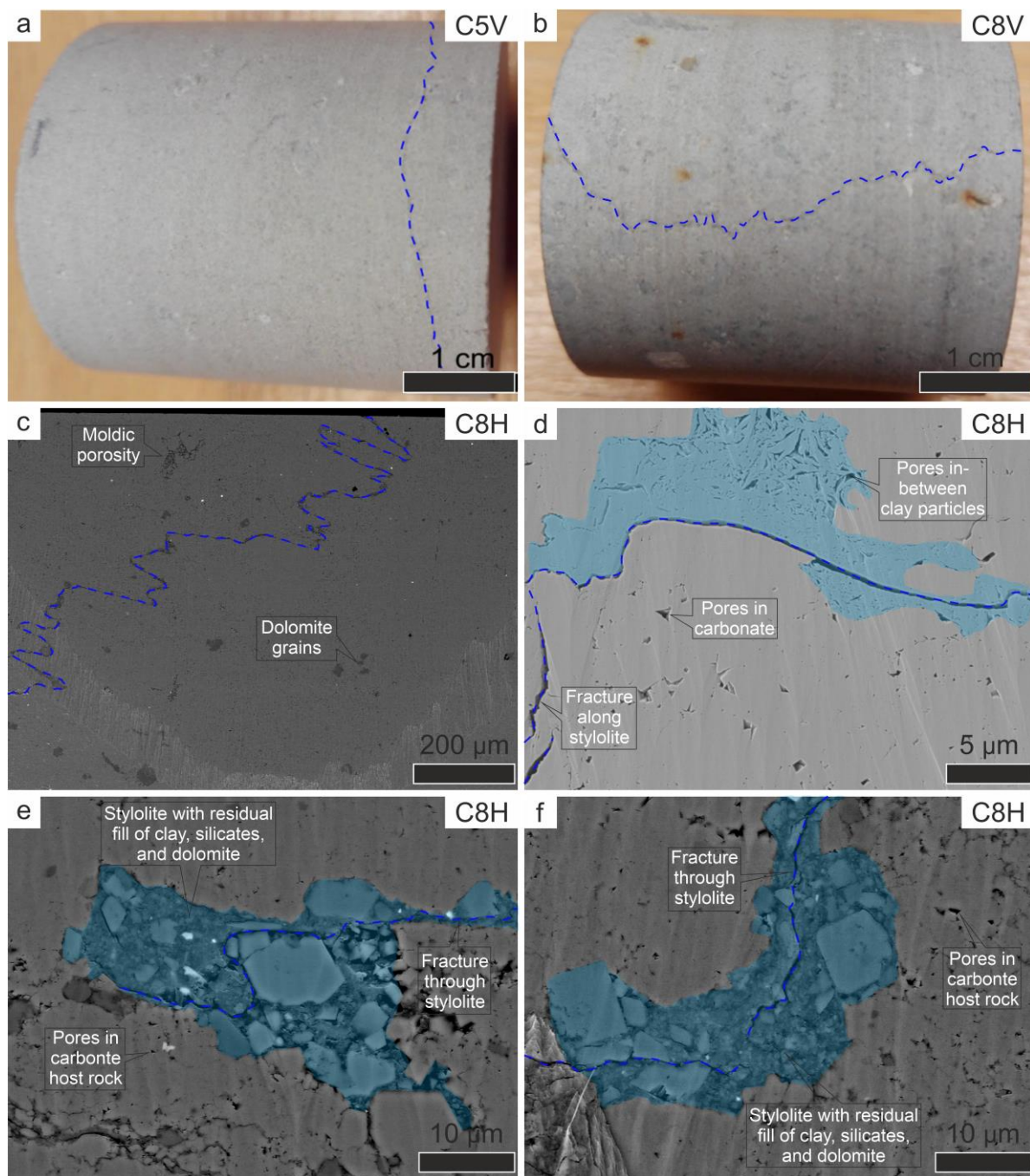


Figure 2: Examples of typical microstructures in analyzed limestone samples with a) and b) showing stylolite planes (highlighted by blue dashed lines) in core plugs, c) SE2 image of stylolite plane in BIB section, d) stylolite plane and interparticle pores in clay, and e) and f) BSE images showing the fracture through the stylolite with residual fill of clays, silicates and dolomite grains containing interparticle and intercrystalline submicron scale porosity, see text for further details.

Figure 2d illustrates the presence of nanoporosity along the stylolite plane in contrast to the almost tight nature of the limestone's matrix containing only few clusters of interparticle nanopores. Insoluble minerals like clay, quartz, dolomite, and denser minerals remaining from dissolution processes accumulated at the stylolites' peak tops contributing to interparticle/intercrystalline nano-/microporosity

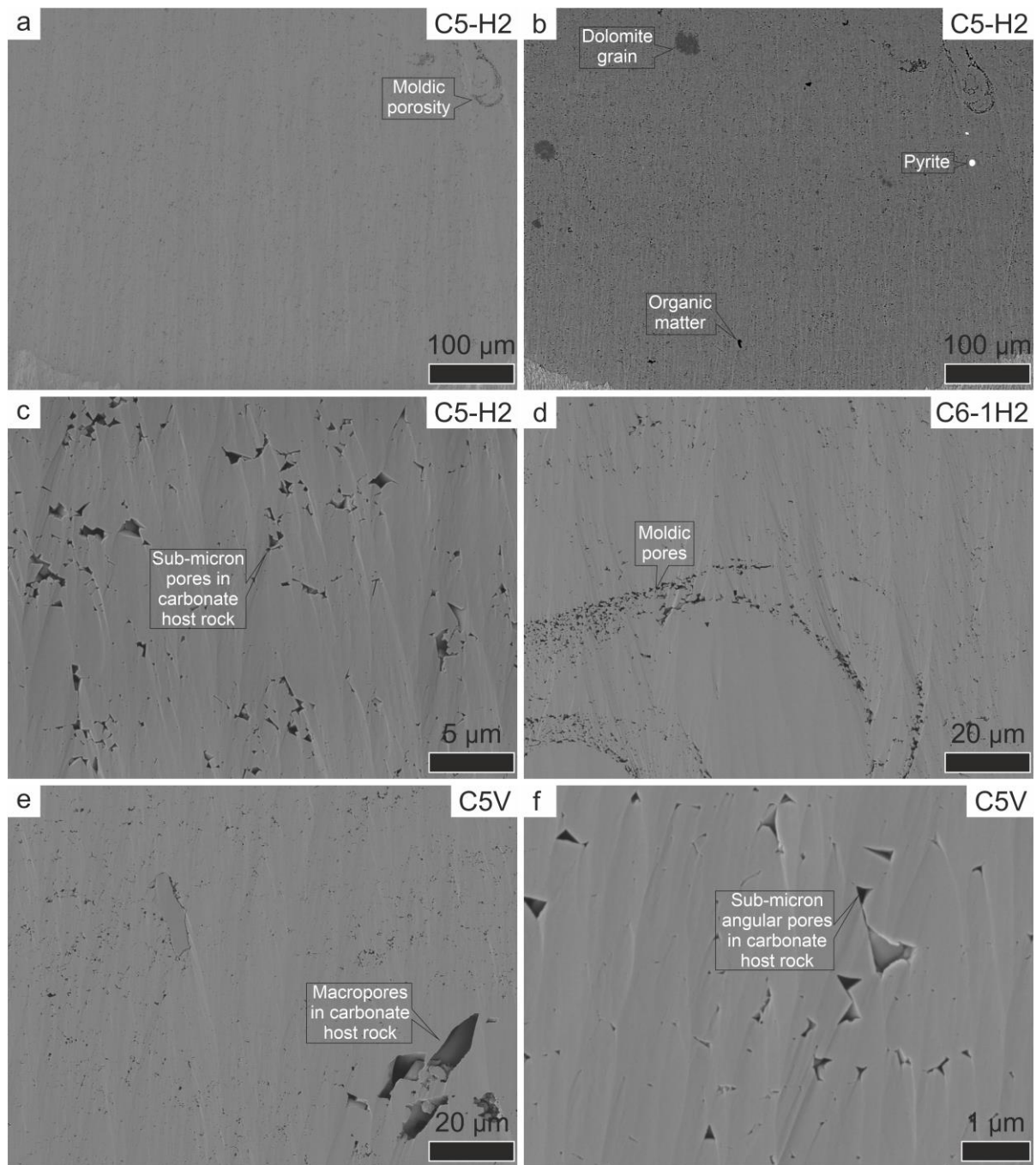


Figure 3: Typical microstructures identified in the samples investigated. a) SE2 image of the BIB-cross-section indicating the low porosity visible at low resolution (pixel size 800nm) and moldic porosity associated with a forminifera. b) BSE image of a) illustrating the homogeneous mineralogy with only a few dolomite grains, pyrite, and organic matter particles. d) SE2 overview images of the visible porosity indicating the submicron scale of the pore sizes. e) SE2 image displaying one of the relatively few macropores detected in the BIB cross-sections. f) High-resolution SE2 image of the typical angular pore geometries in the carbonate host rock.

(Figure 2e and f). Examples of the general microstructure of the thirteen investigated BIB sections are illustrated in Figure 3 showing a completely tight matrix (Figure 3a), a low porous matrix (Figure 3b), matrix with clusters of moldic pores (Figure 3c), and nanoporosity associated with larger fossil remnants (Figure 3d). Besides the moldic pores, the matrix also contains interparticle pores, both being usually

smaller than 1 micron (Figure 3c and d). However, these pores that are associated with partly dissolved fossil remnants recognizable by their specific pore arrangement resembling that of the fossils are not common in the investigated BIB cross-sections (Figure 3d). The BIB cross-sections of C5V and C6-2V (Table 1) also contain some much larger interparticle pores (e.g. Figure 3e) which significantly contribute to the visible porosity. In general, very few but distant macropores were observed. Figure 3f shows the typical microstructure at high resolution showing typical (tri-) angular interparticle and intercrystalline pores relatively close to each other. The smallest visible pores that could be segmented are a few pixels in size.

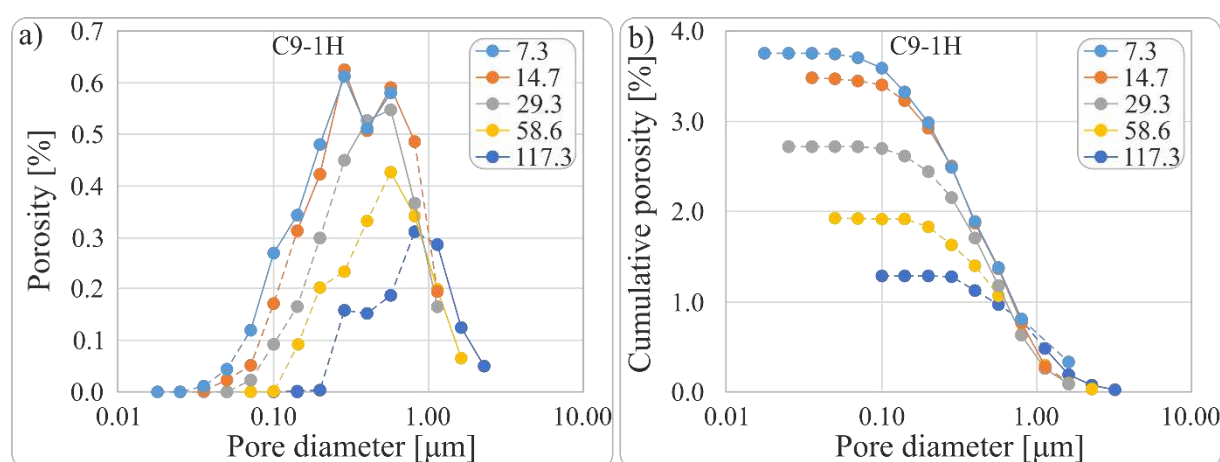


Figure 4: Typical BIB-SEM pore size and porosity distributions of samples quantitatively investigated. (a) Porosity vs equivalent circular pore diameter for the exemplary sample C9-1H at different magnifications distinguished by color. (b) Cumulative porosity versus equivalent circular pore diameter for sample C9-1H. The dashed lines are below the practical pore resolution (PPR) and the color legend corresponds to the pixel sizes related to the magnifications used of respectively 2,500, 5,000, 10,000, 20,000, and 40,000 times.

Overall, the average matrix is characterized by pores mostly in the 100 to 1000 nm pore size range in BIB-SEM (Figure 4b) indicating a general increase of visible nano- and microporosity with magnification. However, the increase stagnates at higher magnification, pointing out that not much additional nanoporosity is expected at higher magnification, or below the practical pore resolution (PPR). This is also validated by uniform pore diameter distributions (Figure 4a), independent from the magnification used. For the permeability estimation via the capillary tube model, the measurements at 14.7 magnification (equal to 20,000x) were applied to improve their detection.

4.2. Pore throat sizes and pore connectivity

In total, 24 samples were analyzed using MICP. The results for the vertical section (Figure 5a) showed a unimodal pore diameter distribution for most samples. The samples B0, B1, B7, B8, and B9 had pore

throat diameters of around 11-15 nm, and samples B2, B3, B4, B5, B6, and B10 had larger pore throats, with diameters of 31-39 μm . The pore throat size distribution of most samples from the horizontal section clearly conforms to each other (Figure 5b). All samples had pore throat diameters of 9-15 nm, except sample B1F which had slightly larger pore throat diameters averaging 23 nm. However, some samples (B1G, B4, and B10) indicate continued mercury intrusion even at the device's maximum pressure, corresponding to the smallest pore diameter of 3 nm (Figure 5). All samples were conformance corrected ($> 4 \mu\text{m}$) for surface irregularities (Newsham et al., 2004; Sigal, 2009). In conclusion, the samples are relatively homogeneous and reflect a narrow pore throat size distribution with small variations between 8 nm and 40 nm and no trends related to fault proximity or bed thicknesses (see Figure 1b for corresponding sample positions relative to the fault).

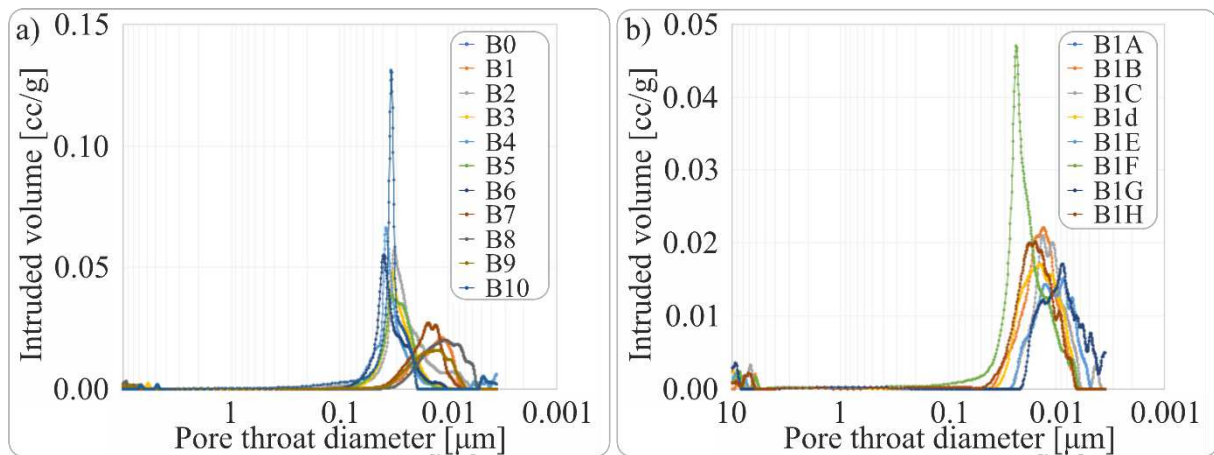


Figure 5: MICP results showing the pore throat size distributions as intruded volume [cc/g] versus equivalent pore throat diameter of the (a) vertical section, and (b) horizontal section.

The MICP breakthrough fits well with BIB-SEM observations on the Wood's Metal injected (LMI-BIB-SEM) samples at 100 and 200 MPa, equivalent to pore throat diameters of approximately 15 and 9 nm (Figure 6).

The sample injected at lower pressure (100 MPa) showed both, filled and unfilled interparticle pores (Figure 6a), indicating a percolating network that was not fully connected at this low pressure. Instead, the samples injected at twice the pressure (200 MPa) showed that virtually all visible interparticle pores were filled with metal (Figure 6b).

Overall, the relatively small variations in pore volume, pore throat sizes, and pore size distribution with varying distances to the fault imply that faulting and fracturing are essentially post-diagenetic.

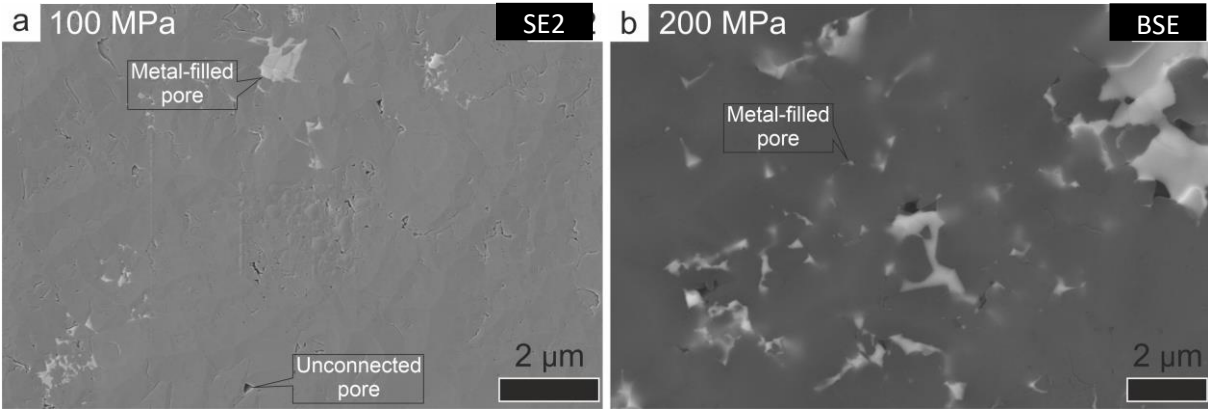


Figure 6: LMI-BIB-SEM result of injected sub samples at (a) 100 MPa and (b) 200 MPa indicating that a significant part is filled with Wood's metal (bright grey) at 200 MPa.

4.3. Porosity

The logged cores show gamma-ray porosities varying between 3.7 to 5.9% (mean $5.0 \pm 0.7\%$) that are slightly higher than porosities derived from He-pycnometry, ranging from 2.5 to 6.0% (average $4.3 \pm 1.0\%$) (Figure 7a&d). The average Archimedes porosities of the beds range from 1.1 to 4.2% (Figure 7b&c and Table 1), with an overall average of $3.0 \pm 0.7\%$. Similar ranges and mean porosities were determined by both, the BIB-SEM- and MICP-methods. The reported porosities of all applied methods originated from the vertical section. Complementary Archimedes-, He-, and MICP-porosities from the same beds and the horizontal section showed comparable porosity variability and no trend towards increased or decreased porosities with distance from the fault (Figure 7e). Hence, we conclude that the bulk matrix porosity is almost homogeneous with an average MICP porosity of 2.9% (1.8 to 4.4%). The visible BIB-SEM porosities are on average 2.9%, varying from 2.1% to 3.5%. Macropores are present, however, they are rather distant from each other in the tight matrix so do not affect the transport properties significantly. Additionally, (micro-) fractures were purposely excluded from the BIB-SEM analyses as our focus was on the microporosity of the matrix.

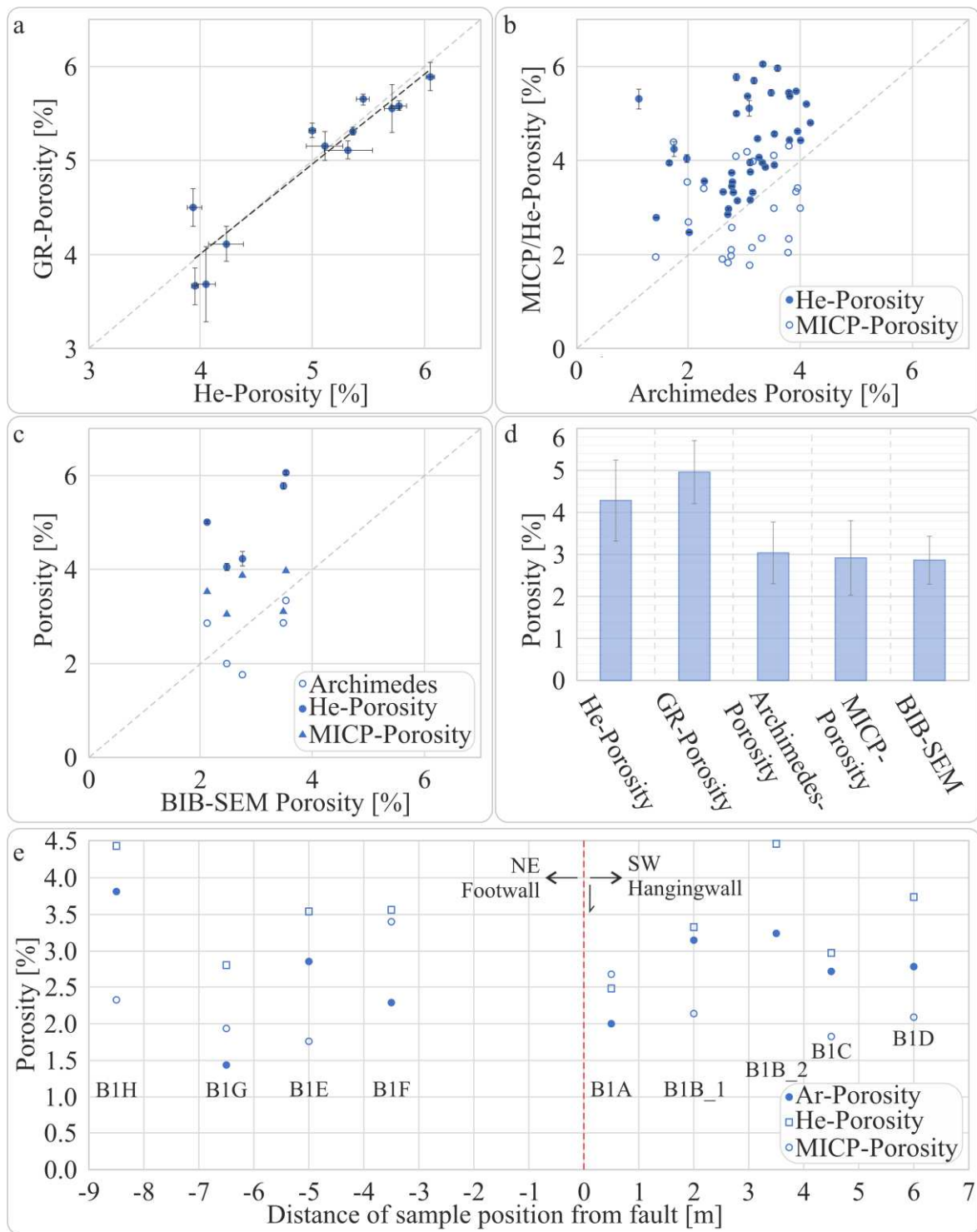


Figure 7: Porosity diagrams. (a) GR porosity vs He-porosity. (b) Archimedes principle porosity vs MICP and He porosity. (c) Archimedes, He and MICP porosity vs BIB-SEM porosity. (d) Comparison of porosity distributions determined by different methods. (e) He, Ar, and MICP porosity evolution with varying distances from the fault (red dashed line).

4.4. Permeability and permeability models

The measured air permeability varies between $1.9\text{E-}18\text{ m}^2$ and $10.8\text{E-}18\text{ m}^2$ with a mean of $(6.8\text{E-}18 \pm 2.1\text{E-}18)\text{ m}^2$. The lowest determined permeability equals the detection limit of the device, at least for air

injection pressures up to ~6.8 bar. A mean of $1.4 (\pm 0.3) \text{ E-17 m}^2$ with a more confined range between 1.2E-17 m^2 and 2.1E-17 m^2 was determined for the same samples, by measurements with argon (Figure 8a). On average the determined air permeabilities are a factor approximately two times lower than the argon permeabilities with no obvious correlation (Figure 8a). No correlation between the measured air permeabilities K_{air} and the maximum hydraulic length l_{max}^h nor the R_{35} representing the pore throat diameter at 35% mercury saturation (Table 1), which were determined by MICP measurements and represent the steepest slope in Figure 5, can be noted (Figure 8b). A similar observation is made for the correlation between the measured argon permeability K_{ar} and the maximum hydraulic length l_{max}^h . In contrast, a positive correlation between measured argon permeabilities K_{ar} and the R_{35} is indicated in Figure 8b. The maximum hydraulic length l_{max}^h thereby varies between 3.7 nm and 23.6 nm among the individual layers with a mean of $15.01 \pm 6.38 \text{ nm}$, while the R_{35} ranges from 4.45 nm to 14.2 nm with a mean of $9.9 \pm 2.7 \text{ nm}$. A lower degree of variation for both the l_{max}^h and R_{35} is observed within layer B1, with values ranging between 6.1 nm and 13.9 nm (mean $8.9 \pm 2.4 \text{ nm}$) and between 6.1 nm and 9.3 nm (mean $7.2 \pm 1.0 \text{ nm}$) respectively.

Correlating air permeabilities (Figure 8c&d) with porosities determined after the Archimedes principle or measured with He-pycnometry (Figure 8c), with MICP and BIB-SEM (Figure 8d) shows no distinct relationship between these properties. This is also true when comparing the porosity results of all four applied methods with the permeabilities measured with argon (Figure 8e).

The highest K_{Air} value was found in layer B0, though, similar to the porosity measurements, no vertical (Figure 8f) or horizontal (Figure 8g) trend towards the normal fault can be identified from the matrix permeabilities of sampled beds. Plug permeabilities from the horizontal section (Bed B1, Figure 8g) consistently show very low values in the range between 7.6E-18 m^2 and 14.3E-18 m^2 (Table 1). Furthermore, results suggest independence from any direction permeability with N-S-, E-W-, and vertical orientation for individual beds was determined (Table 1), hence the rocks are behaving relatively homogeneously and are close to the range of what actually could be measured with the experimental setup.

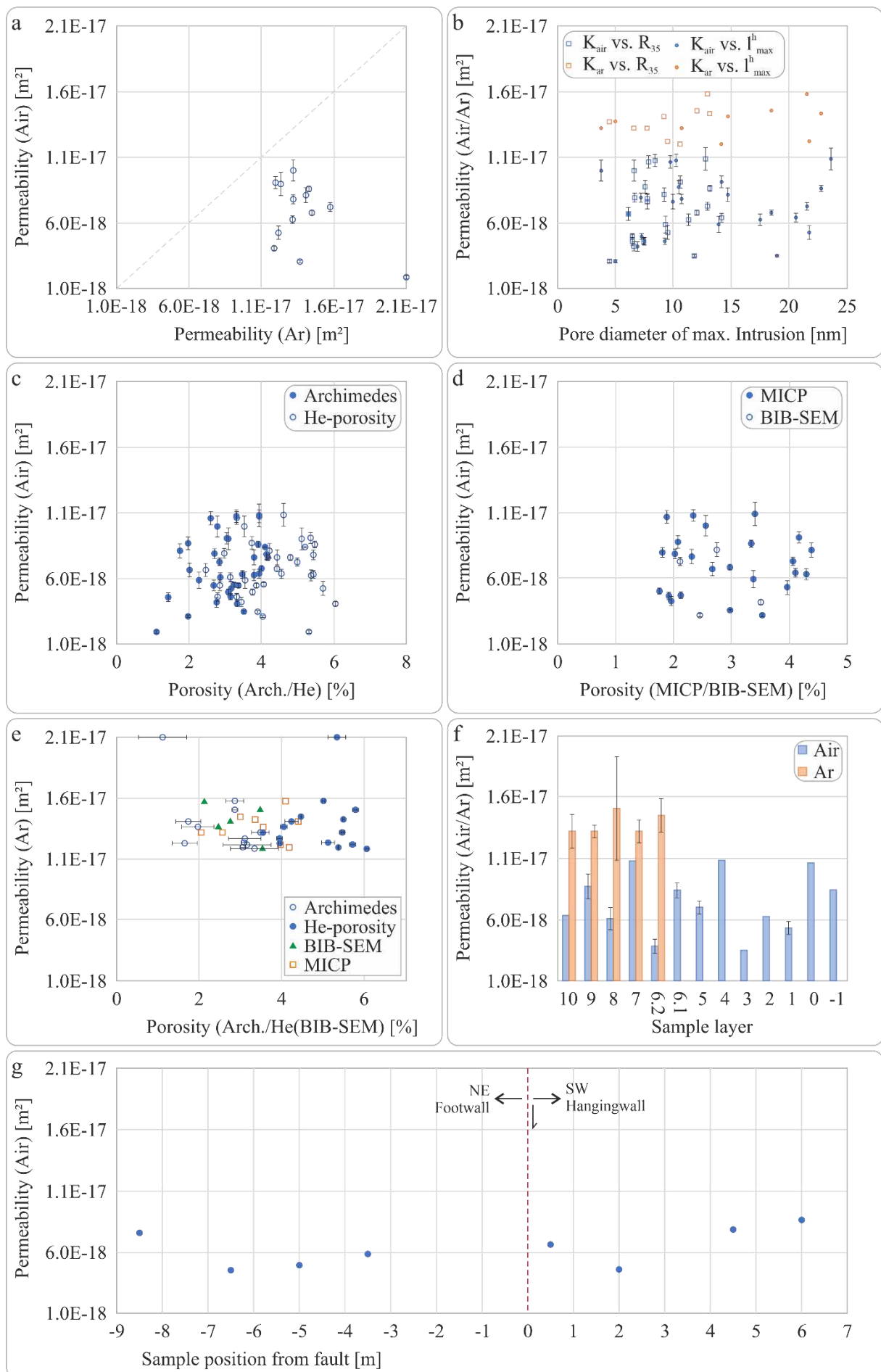
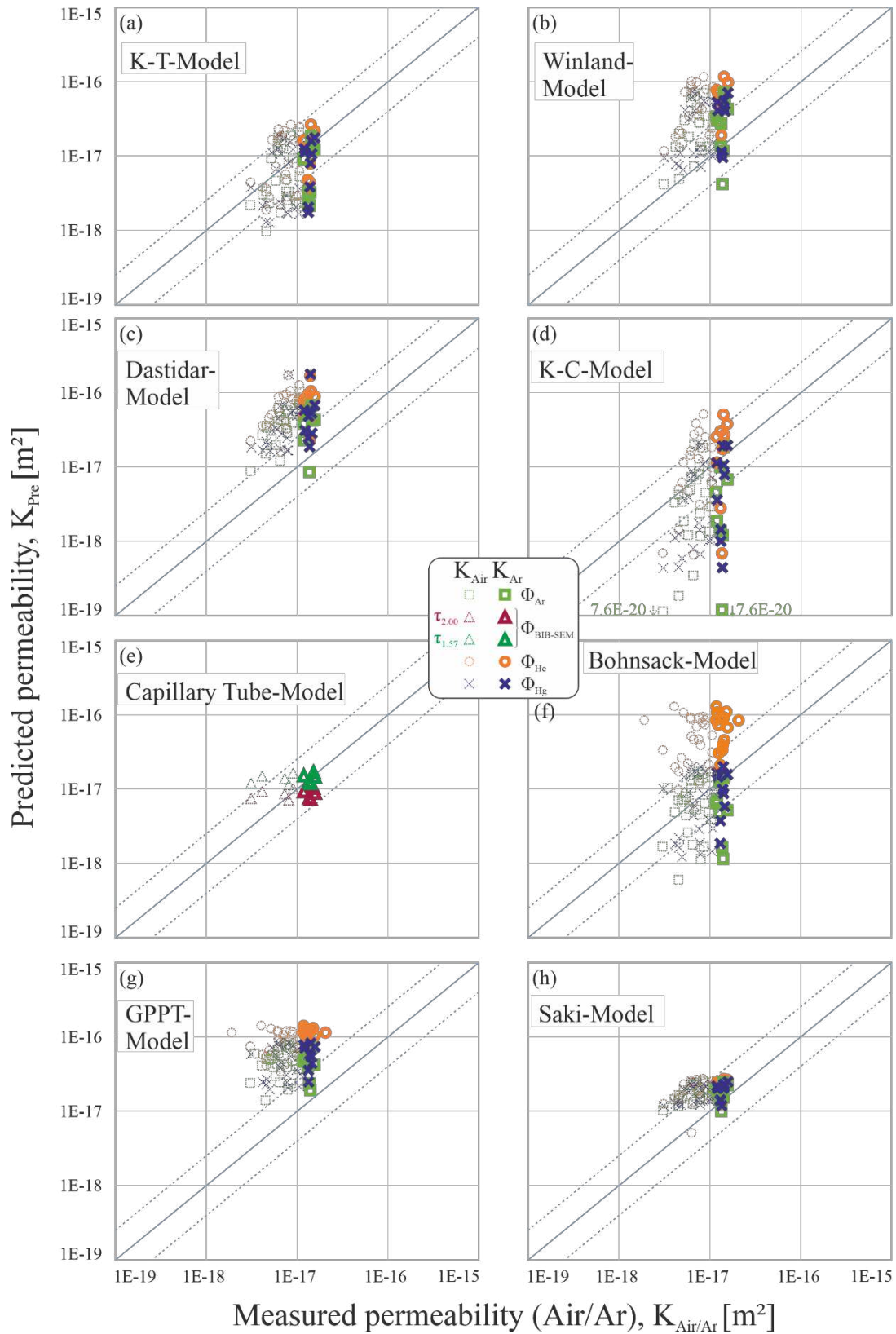


Figure 8: a) correlation between permeability values determined by argon and air measurements, b) permeabilities measured with argon (K_{Ar}) and air (K_{Air}) plotted against the corresponding maximum hydraulic length l_{max}^h (m), where most of the mercury is injected into the sample as well as the R_{35} value, corresponding to the pore diameter at 35% mercury saturation. Air-derived permeability values related to c) porosities determined via the Archimedes principle and He-pycnometry, d) porosities measured by MICP- and BIB-SEM. e) plots the same porosity measurements against argon-derived permeabilities, f) illustrates the Ar-permeability distribution across the sampled layers and g) is showing the permeability variation along bed B1 across a normal fault. See Figure 1b for sample positions in (f) and (g).

All permeability models applied in this study (Figure 9) show at least moderate correlations with measured permeability values. Exception of the Capillary Tube Model (Figure 9e), which is solely based on the BIB-SEM-analysis, we only display permeability prediction models based on Hg-, He-, and Ar-porosities for better clarity, as the GR- and He-porosities, as well as the Ar-, Hg-, and BIB-SEM-porosities, show very low variation among each other (Figure 7d).

Comparing the permeability estimation to the air permeability measurements (K_{Air}), decent fits were achieved for the Katz-Thompson (K-T) Model (Figure 9a), the Winland Model using the Ar- and Hg-porosity (Figure 9b), the Kozeny-Carman Model (K-C) using the best-fit tortuosity factor of $\tau = 1.57$ that was achieved by optimizing the Capillary Tube Model and the He-porosity (Figure 9d), and the Bohnsack Model using the Ar- and Hg-porosity (Figure 9f). Great fits are achieved for the Capillary Tube (Figure 9e) and the Saki Model (Figure 9h), both being well within the 2.5 variance factor from the perfect fit. The Winland Model using He-porosity (Figure 9b), the Dastidar- (Figure 9c), the Bohnsack Model also using He-porosity (Figure 9f), and the GPPT Model (Figure 9g) strongly overestimate the measured permeabilities. While the Kozeny-Carman Model (K-C) using the Ar- and Hg-porosities (Figure 9d) underestimates the air permeability K_{Air} .

In general, similar observations are made when comparing the permeability models to the measured Argon permeabilities (K_{Ar}), although with a better correlation except for the K-T- (Figure 9a) and the K-C Models (Figure 9d). Particularly well permeability estimations are achieved by applying the Capillary-tube (Figure 9e) and the Saki Model (Figure 9h).



530

531 Figure 9: Correlation between measured permeabilities by using air (K_{Air}) or argon (K_{Ar}) as permeating fluid and
532 predicted permeabilities (K_{Pre}) by testing different models: the Katz-Thompson Model (K-T Model) (a), the
533 Winland Model (b), the Dastidar Model (c), the Kozeny-Carman Model (K-C Model) (d), the Capillary Tube
534 Model (e), the Bohnsack Model (Lms) for mud-supported limestones (f), the Global Porosity-Permeability-
535 Transform (GPPT Model) (g), and the Saki Model (h). The dashed lines indicate a variation factor with a value of
536 2.5 from a perfect fit. Except for the capillary tube model (h), permeability measurements and permeability

calculations were done on the same samples and with porosities from the different measurement methods (MICP, He-Pycnometry, Archimedes buoyancy, and BIB-SEM).

4.5. Mechanical properties and relation of petrophysical properties to buried samples

We calculated the Poisson's number, the dynamic Young's Modulus, and the Bulk Modulus from sonic velocity measurements using equations 5, 6, and 7, respectively (Table 2). For samples where the shear

Table 2: Summary of the mechanical parameters of Simmelsdorf quarry limestones (Malm β) calculated from P- and S-wave velocities. ν = Poisson's number; E = Young's Modulus; K = Bulk Modulus

Bed	Horizontal	Bed thickness	Distance from fault	Plug	V _P	V _S	ν	E	K	dV/V**
[#]	[-]	[cm]	[m]	[-]	[m/s]	[m/s]	[-]	[GPa]	[GPa]	[%]
10		55	-	B10_V	5758	3160	0.28	65	51	0.12
				B9_V	5808	3190	0.28	67	52	0.12
				B9_2V	5957	3328	0.27	74	54	0.11
9		22	-	C91V	5486	-	0.27*	62	45	0.13
				C91H	5501	-	0.27*	62	45	0.13
				C92H	5506	-	0.27*	63	45	0.13
				B8_V	5812	3305	0.26	71	50	0.12
8		20	-	C8V	5615	-	0.27*	66	47	0.13
				C8H	5767	-	0.27*	69	50	0.12
7		40	-	B7_V	5845	3298	0.27	71	51	0.12
				C62V	5583	-	0.27*	64	46	0.13
6.2		15	-	C62H1	5604	-	0.27*	65	46	0.13
				C62H2	5725	-	0.27*	67	49	0.12
6.1		35	-	C61V	5735	-	0.27*	69	49	0.12
				C61H2	5403	-	0.27*	61	44	0.14
				B5_V	5730	3275	0.26	69	48	0.13
5		40	-	C5V	5484	-	0.27*	62	45	0.13
				C5H2	5560	-	0.27*	64	46	0.13
				B4_V	5948	3305	0.28	72	54	0.11
4		35	-	B4_2V	5906	3305	0.27	72	53	0.11
3		32	-	B3_V	5849	3338	0.26	73	50	0.12
2		18	-	B2_V	5488	3250	0.23	66	41	0.15
1	D	45	6.0	B1D_V	5991	3385	0.27	76	54	0.11
1	C	45	4.5	B1C_V	5984	3248	0.29	71	57	0.11
1	A	45	0.5	B1A_V	5733	3195	0.27	67	50	0.12
1	F	45	-3.5	B1F_V	5717	3263	0.26	69	48	0.13
1	E	45	-5.0	B1E_V	5866	3453	0.23	77	48	0.12
				B1E_2V	6090	3313	0.29	74	59	0.10
1	G	45	-6.5	B1G_V	6254	3440	0.28	80	61	0.10
1	H	45	-8.5	B1H_V	5977	3298	0.28	72	55	0.11
1		45	-	B1_V	5985	3370	0.27	75	54	0.11
0		30	-	B0_V	6513	3565	0.29	85	66	0.09
-1		43	-	B-1_V	5865	3218	0.28	69	53	0.11

* Mean Poisson's number calculated from samples, where the p-wave (V_P) and the s-wave (V_S) velocity were available

** Percentual change in volume at a burial depth of 3000 m with an assumed confining pressure of dp \approx 60 MPa according to Drews et al. (2019), applying equation 7

velocity was not available and hence, the Poisson's number could not be calculated, the average value of $\nu = 0.27$ derived from the other samples was used. As the samples were analyzed in two different laboratories resulting in similar values, they are expected to be credible. All limestone beds are very homogeneous in terms of geomechanical properties, with the dynamic E- and K Moduli ranging between 65 to 85 GPa with a mean of 73 ± 5 GPa and 41 to 66 GPa with a mean of 53 ± 5 GPa, respectively.

5. Discussion

5.1. Microstructure and pore geometry

Submicron interparticle and intercrystalline pores of sub-angular shape are the most abundant types of pores within the matrix of Malm β limestones. Also, elongated interparticle pores are present, as well as moldic pores, which resulted from the dissolution of the still recognizable fossil remnants but are relatively low in number and can be relatively large in size (Figure 3). While the elongated open void spaces are associated with stylolites that are interpreted to have re-opened due to stress release- and/or desiccation. The pores at the stylolite interfaces alternate with the accumulation of insoluble, dense minerals at mainly their peaks (Figure 2e and f), coinciding with the observations of e.g. Heap et al. (2014) and Toussaint et al. (2018). They assign a complex internal structure of varying thickness to these stylolites, which are interpreted to be a product of the horizontal linkage and vertical coalescence of multiple pressure-solution seams (Nenna and Aydin, 2011; Toussaint et al., 2018). Hence, our findings confirm the porous nature of stylolites, which can significantly contribute to the total porosity of low-porous carbonates, at least under unconfined stress conditions. However, due to their elongated shape, it is reasonable to assume that these structures will successively be closed with increasing effective stress (Si et al., 2018), for the case that principle stress is directed perpendicular to the longitudinal axis of the stylolite and hence, to the elongated pore spaces, which are typically arranged parallel to the stylolites. This assumption is emphasized by the continued mercury intrusion at the device's maximum pressure (Figure 5), reflecting the closure of these pores or of microfractures.

5.2. Pore throat size and pore connectivity

The BIB-SEM porosity, as well as the LMI-BIB-SEM observations regarding the filling of almost the entire visible open pores at high injection pressure (Figure 6), indicate that a significant part, if not all of the BIB-SEM porosity, is connected. This is in good agreement with the similarity of the average BIB-SEM porosity and the average MICP porosity values (Figure 7c&d). Moreover, comparing the mean pore size from BIB-SEM (~500 nm, Figure 4a-e) with mean pore throat sizes from MICP (~11 nm and ~33 nm, Figure 5) results in pore body to pore throat (aspect) ratios of about 25:1. According to Zhao et al. (2018) who also apply MICP, such ratios for tight carbonates are typically in the range of c. 40 to 480, with small ratios indicating increased conductivity to fluid flow compared to large ratios. From our ratio, we assume that the samples have comparatively high permeabilities for tight carbonates. However, the ratio only allows for qualitative statements. For example, Cai et al. (2019) have shown that tortuosity and connectivity, among others, play a significant role in controlling hydraulic flow in porous media. Using the ratio as the sole factor for permeability estimation is therefore not advisable.

5.3. Porosity

A comparison between the various porosity measurement methods shows general conformance among the results with values between 2% and 5% (Figure 7d), and also with published data of the same Malm β stratigraphy (Beichel et al., 2014; Böhm et al., 2010; Bohnsack et al., 2020; Homuth et al., 2014, 2015; Mraz et al., 2018). This observation applies particularly to the GR- and He-porosities with only minor deviations from each other (Figure 7a&d). In contrast, The Archimedes, MICP, and BIB-SEM porosities show uniformly lower porosity values for the same samples (Figure 7d). Various reasons for this deviation can be considered.

Deviation in measured porosity values can be related to limitations of the individual methods, which e.g. might inhibit the detection of micropores. Both methods, the Archimedes isopropanol and the mercury injection method, are limited by the fluid-rock interaction of the intruding fluid, hence the isopropanol and the mercury, respectively. Thereby, mainly the surface roughness, intrinsic (wetting) contact angle of the fluid, the wetting state, and the spatial distribution of wettability appear to control pore-scale fluid occupancy and connectivity (Armstrong et al., 2021). However, as the complex

interplay of these factors is still far from being fully understood (Armstrong et al., 2021), it is yet difficult to quantify its impact on the individual porosity results. The Archimedes isopropanol and mercury injection methods, however, are also limited by the negative or injection pressure, respectively (Giesche, 2006), preventing the detection of pores below a diameter of 3 nm (MICP) and slightly smaller pores (Archimedes method)(Kiula et al., 2014). Particularly the He-pycnometry and Archimedes measurements are prone to small inaccuracies, as air trapped at isolated and dead-end pores might not have been entirely removed during the vacuuming process. In contrast, the bulk Gamma-ray and the BIB-SEM method are not affected by this problem, though the latter method is limited by its maximum resolution which impedes resolving pores below 10nm. However, this should not play a significant role, as it is clear from the pore size distributions of our samples that the majority of pore space is in the 0.1 – 1 μm range (Figure 4a).

the porosity differences could also be caused by the methods' principles. While the GR- and BIB-SEM measurements can detect the total porosity (including isolated pores), all other methods (He-pycnometry, Archimedes method, and MICP) measure the effective porosity. If the sample, for instance, contains a large ratio of isolated mesopores, both the GR- and BIB-SEM methods should provide higher porosities than all the other methods applied. If, however, the sample's porosity consists of mostly open microporosity, both the He- and the GR-methods will result in higher porosity values.

Keeping the individual methods' advantages and disadvantages in mind, our observations indicate a low ratio of isolated pores within the samples' matrix, inferred from the only slight difference between GR- and He-porosities and only few unconnected pores in the LMI-BIB-SEM measurements (Figure 7d). The higher mean porosities from the He-pycnometry and GR-methods compared to the Archimedes, BIB-SEM, and MICP porosities are probably mostly related to the fact that the latter methods either cannot record significant amounts of open pore space (which is the case for the Archimedes method) or (micro-)fracture- and stylolite-associated pore space was excluded from the measurements (which relates to the BIB-SEM method). The MICP method, on the other hand, did most likely not detect the (micro-)fracture- or stylolite-related pore space due to their closure at high confining pressure. Hence,

the He-pycnometry provides the most reliable values for the effective porosity, while the bulk gamma-ray method additionally detects isolated pore space.

As the ratio of microfractures and stylolites is quite low, they presumably do hardly impact the matrix storage capacity. Neither across the sampled limestone section nor along an individual layer (B1), a significant change in the mean matrix porosity was visible (Figure 7e). This suggests that the petrophysical properties can be considered constant in the investigated section.

5.4. Permeability and permeability models

Although fluid flow in tight carbonates is primarily controlled by general occurrence, amount, and type of deformational features such as faults and/or fractures (Al-Obaid et al., 2005; Dimmen et al., 2017; Litsey et al., 1986; O'Neill, 1988; Zeybek et al., 2002), fluid transport into and from the rock matrix should still be considered, particularly in terms of modeling purposes. Therefore, different permeability measurement methods and permeability prediction models will be discussed regarding their reliability and limitations.

5.4.1. Permeability

A large spread in air permeabilities ($1.9\text{E-}18 \text{ m}^2$ to $10.8\text{E-}18 \text{ m}^2$) most likely results from the aforementioned device-related issues of relatively low confining and injection pressures and the missing Klinkenberg correction of the air-permeabilities. It also leads to a significant deviation from the argon permeabilities ($1.2\text{E-}17 \text{ m}^2$ to $2.1\text{E-}17 \text{ m}^2$, Figure 8a). Surprisingly, a missing Klinkenberg correction should rather result in increased than in comparatively lower permeabilities, as it is the case here. No laminar flow may have been established during the air permeability measurements, despite waiting until no large variations could be noted before starting the actual measurements. A similar problem is reported by Bohnsack et al. (2020) for mud-supported limestone, samples that are comparable to ours. Hence, measuring the permeability of tight rocks by using air is apparently less suitable than using argon, which should be investigated in another study.

No relation between measured permeabilities and the maximum hydraulic length l_{max}^h can be found, which holds also true for the correlation between air permeabilities K_{air} and the R_{35} , corresponding to

the pore throat diameter at 35% mercury saturation (Figure 8b). This is mostly related to the strongly confined range of permeabilities and the pore throat diameters l_{max}^h and R_{35} . Nevertheless, a slight positive correlation between the argon permeabilities and the R_{35} is recognized, suggesting its control on gas permeability.

No correlation between porosity and neither air (Figure 8c&d) nor argon permeability (Figure 8e) is identified. We, therefore, suggest that the permeability mostly depends on pore connectivity and the pore throat size distribution rather than on the effective porosity. Smodej et al. (2020) also showed that low permeability is mostly controlled by the smallest pores. Their findings are in accordance with our results, as all investigated samples showed very confined ranges of pore size distribution at the nano- to micropore (0.008-0.04 μm) scale, very low relative permeabilities, and no positive correlation between samples with larger pore diameters (0.03-0.04 μm) and increased permeabilities. No positive correlation between plug-parallel stylolites and permeability was observed. The Smodej et al. (2020) results, although not for tight carbonates, partly contradict results by Heap et al. (2014), which showed that plug-parallel stylolites in mostly homogeneous rock can increase the sample's permeability by about one order of magnitude.

A similar observation applies to fluid flow transverse to stylolites, where no influence could be detected. Varying effects on fluid flow have been reported over the last decades (e.g. Burgess and Peter, 1985; Koepnick, 1987; Korneva et al., 2014; Lind et al., 1993; Rustichelli et al., 2015; Toussaint et al., 2018) and related to mostly the dependence on the type and amount of material collected in the stylolites and the offset of sealing material at teeth (Bruna et al., 2019; Koehn et al., 2016; Toussaint et al., 2018). Furthermore, whether stylolites form barriers or act as conduits for subsurface fluid flow is a complex matter and additionally relies on various factors such as roughness, amount of insoluble and non-permeable constituents, and their distribution on the stylolite's surface, evolutionary stage, or whether the stylolite is still active or not (Bruna et al., 2019). However, as we did neither determine the amount of insoluble constituents nor whether the stylolites were still active or not, our findings do not allow for conclusions regarding these aspects. Nevertheless, it is most likely that the stylolite filling has a comparable low permeability as the carbonate matrix, as the microstructure of the stylolite filling (Figure

2d) is typical for porous clays or claystones with permeabilities in the same order of magnitude. Hence, no permeability anisotropy of the bulk rock is to be expected and could also not be observed.

Overall, faulting and fracturing did not noticeably affect the permeability of the surrounding protolith, at least at the scale of investigation. We relate this to the low permeability, which inhibits intensive fluid-rock interactions due to the negligible exchange of the percolating fluid. Therefore, permeability alteration was either restricted to only a very limited area around the fault, or more likely, faulting and fracturing occurred after the intense compaction and diagenesis.

5.4.2. Permeability Models

As illustrated in Figure 9, most applied permeability prediction models correlate relatively well with the measured permeabilities (K_{Ar} and K_{Air}). However, except for the capillary tube- and the Saki-model, the variation of the predicted permeabilities K_{Pre} is at least one order of magnitude. As permeabilities measured with argon are only about twice as high as measured with air (Figure 8a), the correlation-difference between those methods is low with a slight shift of the K_{Air} towards lower permeability values. Still, some models such as the capillary tube- and the Saki Model show a better correlation to measured permeabilities independent from the applied gas than the other models.

A possible cause for the deviation of the K-T Model results from the measured permeabilities (Figure 9a) might be related to the empirically determined constant C of 1013/89 (Rashid et al., 2015), which was calibrated on different rocks, though still tight carbonates like the samples used in this study. Furthermore, also the missing correlation between the K-T Model's main influencing factor, the maximum hydraulic length l_{max}^h , and both measured permeabilities might partly be responsible for the models' deviation from the measured permeabilities. Nevertheless, a good prediction of permeability by applying this model can be achieved. A larger range of permeabilities, maximum hydraulic lengths, and porosities would be needed for a more confident statement on the models' prediction performance.

Although the Winland Model applies the R_{35} factor, which seems to influence the measured permeability (Figure 8b), its correlation with the measured permeability is relatively poor (Figure 9b). We relate this to a similar reason as for the previous model, as it integrates three constants (C_w , a_1 , and a_2) that were

calibrated on a specific data set (Comisky et al., 2007; Gunter et al., 2014; Rashid et al., 2015), to the confined range in permeability and R_{35} values, as well as to the observation that the three empirical constants' influence has more impact than the R_{35} value.

The overestimation of the permeabilities predicted with the Dastidar Model (Figure 9c) might be related to the fact that it applies a weighted geometric mean of the pore throat radius which integrates the full range of effective porosity. However, various studies have already shown that permeabilities in tight limestones are rather controlled by the pore throat radii (Cai et al., 2019; Zhao et al., 2018) or the smallest pore body sizes (Smodej et al., 2020) rather than by the entire effective porosity range.

The permeability values calculated after the Kozeny-Carman-model (K-C Model) are among others dependent on the tortuosity factor τ , which was determined from fitting the Capillary Tube Model based on the BIB-SEM measurements and is thought to be highly accurate. The yet large spread in results could be related to inaccuracies in the tortuosity factor determination due to a low sample volume that was analyzed (Figure 9d). However, as this factor seems to be quite accurate for the examined very homogeneous limestones, indicated by the great correlation of the also tortuosity-dependent Capillary Tube Model with the measured permeabilities, a different reason must be responsible for the only moderate permeability estimation by the K-C Model. We think that it is rather related to the specific surface area S_0 , which was measured with the MICP. As mentioned earlier, this property might be underestimated at high injection and confining pressure due to the closure of microfractures and stylolites, therefore resulting in inaccurate permeability predictions. Measuring the specific surface area with a gas sorption system (BET-method) or additionally with BIB-SEM should give better permeability prediction values.

In contrast to the previously discussed permeability prediction models, the Capillary Tube Model correlates very well, particularly with the measured argon permeabilities (Figure 9e), but also quite well with air permeabilities. As all parameters needed for permeability calculation applying the Capillary Tube Model were derived from the investigated samples, which is significantly different from the other permeability prediction models, a very good fit was to be expected. Also, as this model does neither integrate additional empirically determined constants nor porosity values from any of the applied

porosity measurement methods, the calculated permeability should correlate well with the measured permeability if the tube model is applicable. The very low deviation from the measured permeabilities (Table A- 1) confirms the model's applicability.

The decent correlation between measured permeability data and values calculated after the Bohnsack Model (Figure 9f) is most likely related to the fact that the permeability model was calibrated on measured porosities and permeabilities of mud-supported limestone cores, derived from the same stratigraphic unit as the one investigated in this study (Bohnsack et al., 2020). Hence, despite the large spatial distance of these samples, their petrophysical comparability seems to be given, which has already been noticed by Homuth et al. (2014, 2015) and Mraz et al. (2018), as they determined petrophysical values in a similar range to that of our rock samples and those of Bohnsack et al. (2020), but derived from sampling points located farther to the north of the South German Molasse Basin.

Similar to the Dastidar Model, the GPPT Model clearly overestimates the measured permeabilities (Figure 9g). This model was calibrated on more than 400 limestone samples and depends on only two variables, namely the effective porosity and the rock fabric number, which is a specific number associated with different types of lime- or dolostones (Lucia, 1995, 2001). We assume that the overestimation is related firstly to the wide range and large number of lime-/dolostone samples used for the model calibration, which led to the integration of four empirical constants. Secondly to the rock fabric number, which implies that the type of pore structure and connectivity is similar for each lithology type, however, this is highly unlikely. And thirdly to the effective porosity, which is not well suited for predicting permeabilities due to the below discussed reason.

A very good correlation between predicted and measured permeabilities is achieved when applying the Saki Model (Figure 9h). This model depends on the porosity, the smallest pore/throat radius R_{35} , and three empirically determined constants (Saki et al., 2020). The fact that both the Winland- and the Saki Model use the R_{35} parameter, which shows a slightly positive trend with particularly the argon permeability (Figure 8b), with the latter model correlating better with the measured permeabilities implies that the calibration samples used by Saki et al. (2020) are more closely related to the samples investigated in our study than the ones used by Winland (Comisky et al., 2007; Gunter et al., 2014;

Rashid et al., 2015). Whether this model represents the best permeability estimation model for tight carbonates, in general, is therefore questionable and has to be investigated in further studies on other tight carbonates.

Implications for matrix permeability controlling factors

From the observations of the application of differently measured porosities, we can conclude that microporosity does not have a significant impact on the rock matrix' permeability. This is indicated by the overestimation of predicted permeabilities that use the more accurate He-porosity values. As the He-porosity, which is higher compared to the Ar-, Hg-, and BIB-SEM-porosities due to the capturing of microporosity, is integrated as multiplication factor (K-T-model) with exponential factor (Winland-, Dastidar-, K-C-, and Bohnsack Model), or as logarithmic factor (Saki- and GPPT Model), the predicted permeabilities are also elevated. With these permeability predictions deviating from the measured permeabilities, a negligible effect of the microporosity, but also a higher importance of the pore throat size distribution can be inferred, which has also been concluded by Lala and El-Sayed (2017). In particular, the pore throat radius at a mercury saturation of 35% (R_{35}) seems to be the radius contributing most to the fluid flow in the pore network, as both well-performing models (Winland and Saki) integrate this parameter. Also, a correlation between argon permeabilities and the R_{35} could be found, though without a clear trend due to the confined range in values (Figure 8b).

From the comparison, we can further conclude that most permeability prediction models deviate from the measured permeabilities due to empirically determined variables that were calibrated on individual rock sample sets from other locations and of slightly different lithological types. But also due to the application of the effective porosity as sole physical input parameter, which is not the main permeability-controlling factor according to Cai et al. (2019) and Zhao et al. (2018). Fluid flow in pore networks also strongly depends on the wettability of the permeating fluid/gas, the spatial distribution of the wettability which is related to the minerals present in the sample, as well as on the surface roughness (Armstrong et al., 2021). Both the spatial wettability distribution and the surface pore roughness are difficult to quantify and were not available in this study. This fact and the complex interrelation of these factors impede reliable permeability predictions, as most permeability prediction models applied in this study

– except for the Capillary Tube and the Bohnsack Model – try to approximate the permeability based on mercury-derived pore throat diameter distributions, which in turn depend on the permeability-controlling factors stated by Armstrong et al. (2021). As these factors also concern the permeability measurement itself, the permeability prediction derived from measurements that use different permeating fluids will always be prone to inaccuracies unless detailed information on the wettability distribution, the fluid's wettability, and the surface roughness of the sample is considered.

Model Rating

To quantitatively identify the best-performing model for permeability estimation, the Mean Residual Square Error (MRSE) was calculated for each model and each porosity-determining method (Table A-1) as illustrated in Figure 10. We will compare only our rankings regarding the models' performances in relation to the argon permeabilities to the rankings of other authors from here on, as the argon permeabilities are more reliable than the air permeabilities.

Based on the MRSE, a ranking for each method and an overall comparative ranking could be determined (Table A-1), where the Capillary Tube Model could not be taken into account directly as it does not use a bulk porosity method. Relating the permeability predictions to the measured air permeabilities K_{air} (Figure 10a) gives satisfying results for the K-T- (overall rank 1), the Saki- (overall rank 2), and the Bohnsack Model (overall rank 3). A slightly different rating results from models using Φ_{Ar} and Φ_{Hg} , where both the K-T- (rank 1) and the Bohnsack Model (rank 1) perform equally well, and the Saki Model (rank 3) a little worse (Figure 10b). While the comparison to the more reliable measured argon permeabilities K_{ar} shows best correlations with the Saki- (overall rank 1), the Winland- (overall rank 2), and the K-T Model (overall rank 3) achieving slightly lower rankings. Again, a different ranking order results when only considering models applying Φ_{Ar} and Φ_{Hg} , where the Saki Model (rank 1) performs best. The Winland Model (rank 2) as well as the Bohnsack- and the K-T-Model (both rank 3) also show good correlations with the measured argon permeability. The capillary tube Model is always among the top four prediction models. Hence, we suggest using either the Saki Model, which always reliably predicts the measured permeability, or the Capillary Tube Model for estimating the permeability of similar sample lithologies.

Comparing our internal permeability estimation model ranking to those of Comisky et al. (2007) and Rashid et al. (2015) we partly found similarities, although different permeability estimation models were applied in each study. Comisky et al. (2007) for instance found a good correlation between measured and modeled permeabilities after the K-T-method (rank 2) and the Winland method (rank 5). Both models also perform well with our measured permeabilities.

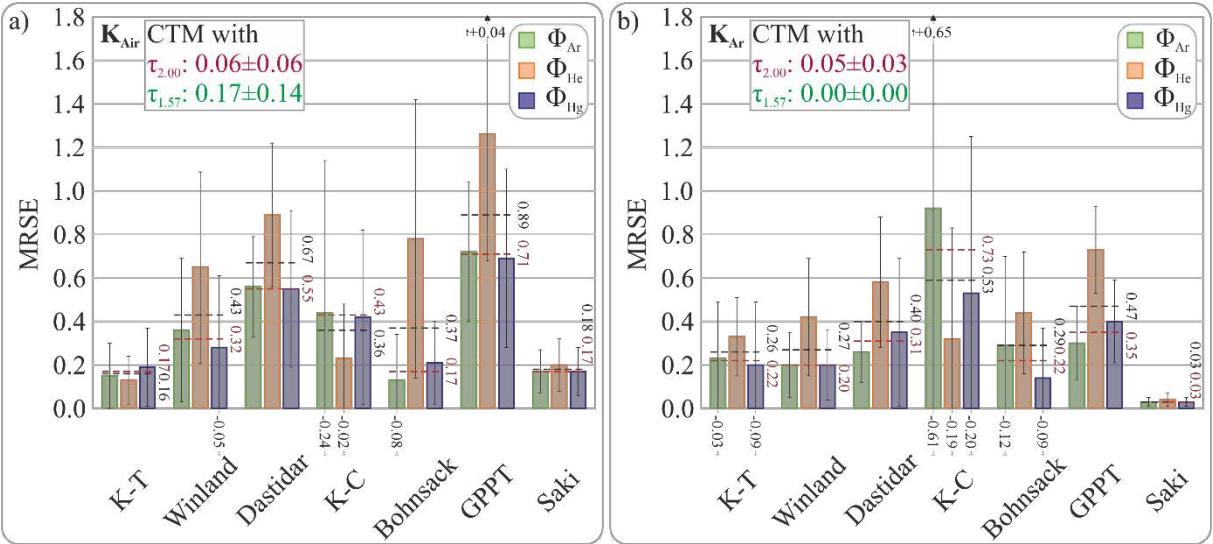


Figure 10: Boxplots of the mean residual square error (MRSE) in relation to a) the corresponding air permeabilities K_{Air} and b) argon permeabilities K_{Ar} for each model and the application of different methods for porosity determination (Φ_{Ar} , Φ_{He} , Φ_{Hg}). The corresponding standard deviations are indicated by vertical black bars. If standard deviations are out of diagram range, the missing values are indicated. The mean MRSE of each model applying across all porosities and across only Φ_{Ar} and Φ_{Hg} are highlighted as black and red lines with corresponding values, respectively. The corresponding values are listed in Table A- 1.

According to Rashid et al. (2015), the four best-performing permeability estimation models are the generic, the RGPZ (Glover et al., 2006) empirical carbonate, the RGPZ approximate theoretical, and the RGPZ exact theoretical model. However, as all four of those models use the grain size as an input parameter, which was not available in our study, we could not confirm or disprove their findings. Those models that were applied by both our study and that of Rashid et al. (2015) are the Winland (their rank 4), the K-T- (their rank 9), and the Dastidar Model (their rank 12). Although a comparison of their ranking results to our ranking is hardly representative, their relative ranking order differs from ours, as the K-T Model performs very well with our data set. Nevertheless, even the best-performing permeability estimation model (generic model) according to Rashid et al. (2015) still has a mean residual square error of 0.402 and therefore shows a poorer correlation to measured permeabilities than the Capillary Tube and the Saki Model. As every comparative study results in a different ranking, a more

profound and comprehensive study integrating a large number of worldwide distributed tight carbonate samples needs to be conducted in the future.

Implications for future petrophysical analyses of tight carbonates

We conclude from our measurements that porosity data for permeability models are best determined by mercury intrusion porosimetry, as this provides not only information on the porosity (the connected pore volume relative to the bulk rock volume) but also on the pore throat size distribution which is primarily controlling the matrix permeability (particularly the R_{35}) and, therefore, required for a reliable permeability estimation. Although a larger pore-size range is accessed and measured through the application of the Helium pycnometry, the mercury intrusion porosimetry method offers a wider range of applicability as also the permeability can be estimated quite accurately, even from small sample volumes such as, for instance, drill cuttings. Hence, even when sample material is limited, the rock's matrix permeability can be estimated, which is particularly useful for subsequent modeling purposes. However, special care should be taken on the presence of microfractures induced by sample handling, ideally one should investigate the sample after injection, for example by employing LMI-BIB-SEM, as this method is suited for the detection of microfractures.

5.5. Mechanical properties and relation of petrophysical properties to buried samples

All samples that were investigated in terms of their rigidity showed similar values in the range between 65 and 86 GPa (Young's Modulus, Table 2). The rock's stiffness, thereby, depends mostly on the pore type, pore geometry, and the total porosity (Eberli et al., 2003; Li et al, 2018, 2018; Weger et al., 2004). Which, together with pre-existing zones of weaknesses such as stylolites (e.g. Agosta et al., 2015; Antonellini et al., 2008, 2014; Graham et al., 2003; Micarelli et al., 2005; Tondi, 2007) and the *in situ* effective stress conditions controls the deformation mode and the resulting fault zone structure with its associated capacity to conduct fluids (e.g. Antonellini et al., 2008; Michie, 2015; Sagi et al., 2016). The majority of the samples' pores were found to be of submicron interparticle, intercrystalline, and occasional moldic small mesoporous type, and of (tri-) angular pore geometry. In combination with the low total porosity, the very high mechanical strength of the investigated rocks can be explained, as all determined properties support a high rock strength (Eberli et al., 2003).

Relating the mechanically very competent limestones to reservoir depths, which in case of the South German Molasse Basin is about 3000 m (Mraz, 2019), a relative volume change of only 0.09 to 0.15% is to be expected. Thus, stress conditions at reservoir level should hardly influence the petrophysical properties of the limestone matrix. Rock matrix petrophysical properties measured at surface conditions should therefore be relatable to stress conditions at reservoir level. Lower porosities measured by Bohnsack et al. (2020) at 30 MPa confining stress (~2.0%) compared to the porosities measured at atmospheric conditions (~3.3%) by Homuth et al. (2014) and by us (2.9-3.2%) of the same stratigraphic unit can be related to changes in lithology, different degrees of dolomitization related to regional heterogeneities of the depositional system, and variation in diagenetic alteration processes (Bohnsack et al., 2020). As the differences in porosities are very low, these factors are thought to play a minor role in their influence on the petrophysical properties at least in the case of Malm β carbonates. Also, as according to our findings, the pore throat distribution is controlling the matrix permeability rather than the effective porosity, these small differences in porosity should be negligible and can be considered as intrinsic sample heterogeneity. Unfortunately, neither information on the pore throat distribution nor permeability measurements at reservoir conditions of Malm β limestones are available. Yet, we are confident that our results reflect a good estimation of in-situ petrophysical properties due to the rocks' high stiffness. Moreover, significant amounts of fluid flow measured in the field are likely to solely relate to the presence of fractures and faults on a larger scale.

6. Conclusion

In this study, petrophysical properties and microstructures of tight carbonates were investigated with various methods, aiming for characterizing the matrix properties of the Upper Jurassic (Malm β) limestones in Northern Bavaria for modeling purposes and deriving correlations between the different measurements using various models. Furthermore, their interdependence of the protolith's porosity with stylolitization and normal fault distance were examined. The overall average porosity measured by MICP-, He-, GR-, BIB-SEM and Archimedes methods is $3.1 \pm 0.96\%$ and the overall average permeability is $1.4\text{E-}17 \text{ m}^2$, confirming tight carbonates. No significant impact of stylolites on the permeability and porosity under confined conditions was observed. Furthermore, no improved

petrophysical properties in a preferred direction were recorded, indicating a homogeneous, isotropic behavior of the rock. Normal faulting had no observable impact on the matrix's poro-perm properties at the meter scale. We, therefore, assume post-diagenetic fracturing and faulting, as otherwise faulting-related processes would have altered the petrophysical properties of the rock matrix. Few leached pores were observed, but with negligible effect on porosity and permeability. The majority of the porosity is in the submicron range. Two models for estimating permeability from porosity and pore size distribution data, obtained from either the MICP- or the BIB-SEM-method, gave very satisfying results compared to measured permeabilities (air and argon) for the examined rock types, namely the Capillary Tube Model and the Saki Model. The Capillary Tube Model applies a tortuosity factor of 1.57 fitted from BIB-SEM analyses, while the Saki Model integrates the pore throat size at 35% mercury saturation. We found that the pore throat diameter is a main factor controlling fluid flow in the rock matrix rather than the effective porosity or the microporosity. The application of the models developed by Katz-Thompson (K-T), Winland, and Bohnsack et al. using Ar- and Hg-porosities also results in reasonable permeability estimations. Due to the rocks' high stiffness of ~73 GPa for Young's Modulus and ~53 GPa for the Bulk Modulus, our findings can be reliably transferred to reservoir conditions.

7. Declarations

7.1 Authors' contributions

SF conducted the sampling, sample preparation, as well as large parts of the petrophysical measurements (Arch.-porosity, parts of He-porosity, MICP-porosity, Air permeability, geomechanical parameters, and permeability modeling), data analysis, and interpretation. He also was primarily responsible for drafting this work. JK conducted the LMI- and BIB-SEM measurements as well as parts of the permeability modeling (Capillary Tube Model) and contributed significantly to the data analysis, data interpretation, drafting, and structuring of this work. IM conducted parts of the petrophysical measurements (MSCL and parts of He-porosity) and helped improve the quality of this work. NK substantially contributed by providing access to the MSCL and thoroughly revising and structuring this work. JU significantly helped improve the quality of this work by designing and revising the manuscript. HS substantially contributed

by thoroughly revising and structuring this work. WB significantly helped improve the quality of this work by revising the manuscript. JS substantially contributed by thoroughly revising this work.

7.2 Acknowledgements

We sincerely want to thank Richard Bärnreuther, his staff, as well as the whole PERMEA-team for providing access to the sampling area and for their strong support. Also, the assistance of Lothar Ahrensmeier, Werner Kraus, Robert Sobott, and Alexandra Amann helped significantly with processing the samples and the petrophysical analysis.

7.3 Competing Interests

All authors declare that they have no conflicts of interest.

7.4 Availability of data and materials

The datasets used and/or analyzed during the current study are available from the corresponding author on reasonable request.

7.5 Ethics approval and consent to participate

This research does not involve any human subjects, human material, or human data.

7.6 Funding

This project was funded by the federal Ministry of Education and Research (BMBF) within the technical programme „GEO:N – Geoforschung für Nachhaltigkeit“ project “PERMEA” (grant no. 03G0865D).

8. References

Abell A, Willis K, Lange D. Mercury intrusion porosimetry and image analysis of cement-based materials. *Journal of colloid and interface science*. 1999;211:39-44.

Agosta F, Wilson C, Aydin A. The role of mechanical stratigraphy on normal fault growth across a Cretaceous carbonate multi-layer, central Texas (USA). *Italian Journal of Geosciences*. 2015;134:1-19. <https://doi.org/10.3301/IJG.2014.20>.

934 Akanji L, Nasr G, Bageri M. Core-scale characterisation of flow in tight Arabian formations. *Journal of*
 935 *Petroleum Exploration and Production Technology*. 2013;3(4):233-41.

936 Al-Obaid R, Al-Thawad FM, Gill HS. Identifying, characterizing, and locating conductive fault(s):
 937 Multiwell test analysis approach. In: *SPE Asia Pacific Oil & Gas Conference and Exhibition, Jakarta,*
 938 *Indonesia, 5-7 April 2005*. 2005.

939 Antonellini M, Tondi E, Agosta F, Aydin A, Cello G. Failure modes in deep-water carbonates and their
 940 impact for fault development: Majella Mountain, Central Apennines, Italy. *Marine and Petroleum*
 941 *Geology*. 2008;25:1074-96. <https://doi.org/10.1016/j.marpetgeo.2007.10.008>.

942 Antonellini M, Petracchini L, Billi A, Scrocca D. First reported occurrence of deformation bands in a
 943 platform limestone, the Jurassic Calcare Massiccio Fm., northern Apennines, Italy. *Tectonophysics*.
 944 2014;628:85-104. <http://dx.doi.org/10.1016/j.tecto.2014.04.034>.

945 Armstrong RT, Sun C, Mostaghimi P, Berg S, Rücker M, Luckham P, Georgiadis A, McClure JE.
 946 Multiscale characterization of wettability in porous media. *Transport in Porous Media*. 2021;140:215-
 947 40. <https://doi.org/10.1007/s11242-021-01615-0>.

948 Bachmann GH, Müller M. Sedimentary and structural evolution of the German Molasse Basin. *Eclogae*
 949 *Geologicae Helvetiae*. 1992;85:519-30. <https://doi.org/10.5169/SEALS-167019>.

950 Bachmann G, Müller M, Weggen K. Evolution of the Molasse Basin (Germany, Switzerland).
 951 *Tectonophysics*. 1987;137:77-92.

952 Barri AA, Hassan AM, Aljawad MS, Mahmoud M. Effect of treatment conditions on matrix stimulation
 953 of carbonate rocks with chelating agents. *Arabian Journal for Science and Engineering*. 2021;1-14.
 954 <https://doi.org/10.1007/s13369-021-05633-4>.

955 Beichel K, Koch R, Wolfgramm M. Die Analyse von Spülproben zur Lokalisierung von Zuflusszonen
 956 in Geothermiebohrungen. Beispiel der Bohrungen Gt Unterhaching 1/1a und 2. (Süddeutschland,
 957 Molassebecken, Malm). *Geol. Bl. NO-Bayern*. 2014;64(1-4):43-65.

958 Berryman JG. Effective stress for transport properties of inhomogeneous porous rock. *Journal of*
959 *Geophysical Research*. 1992;97(B12):17409-24. <https://doi.org/10.1029/92JB01593>.

960 Böhm F, Koch R, Höferle R, Baasch R. Der Malm in der Geothermiebohrung Pullach Th2 -
961 Faziesanalyse aus Spülproben (München, S-Deutschland). *Geol. Bl. NO-Bayern*. 2010;60(1-4):79-112.

962 Bohnsack D, Potten M, Pfrang D, Wolpert P, Zosseder K. Porosity–permeability relationship derived
963 from Upper Jurassic carbonate rock cores to assess the regional hydraulic matrix properties of the Malm
964 reservoir in the South German Molasse Basin. *Geothermal Energy*. 2020;8(12):1-47.

965 Bruna P, Lavenu A, Matonti C, Bertotti G.. Are stylolites fluid-flow efficient features?. *Journal of*
966 *Structural Geology*. 2019;125:270-77.

967 Burgess C, Peter C. Formation, Distribution, and Prediction of Stylolites as Permeability Barriers in the
968 Thamama Group, Abu Dhabi. In: *SPE Proceedings Middle East Oil Technical Conference and*
969 *Exhibition, Bahrain, 11-14 March 1985*. 1985.

970 Cai J, Zhang Z, Wei W, Guo D, Li S, Zhao P. The critical factors for permeability-formation factor
971 relation in reservoir rocks: Pore-throat ratio, tortuosity and connectivity. *Energy*. 2019;188:1-10.

972 Carman P. Fluid flow through granular beds. *Chemical Engineering Research and Design*. 1937;75:32-
973 48.

974 Clarkson CR, Solano N, Bustin RM, Bustin AMM, Chalmers GRL, He L, Melnichenko YB, Radliński
975 AP, Blach TP. Pore structure characterization of North American shale gas reservoirs using
976 USANS/SANS, gas adsorption, and mercury intrusion. *Fuel*. 2013;103:606-16.

977 Cohen KM, Finney SC, Gibbard PL, Fan J-X. The ICS International Chronostratigraphic Chart,
978 International Commission on Stratigraphy. 2013(updated 2022);36:199-204.
979 <http://www.stratigraphy.org/ICSchart/ChronostratChart2022-2.pdf>.

980 Comisky JT, Newsham KE, Rushing JA, Blasingame TA. A Comparative Study of Capillary-Pressure-
981 Based Empirical Models for Estimating Absolute Permeability in Tight Gas Sands. In: *SPE Annual*
982 *Technical Conference and Exhibition, Anaheim, California, U.S.A., 11-14 November 2007*. 2007.

983 Dastidar R, Sondergeld C, Rai C. An improved empirical permeability estimator from mercury injection
 984 for tight clastic rocks. *Petrophysics*. 2007;48(3):186-90.

985 Dimmen V, Rotevatn A, Peacock DCP, Nixon CW, Nærlund K. Quantifying structural controls on fluid
 986 flow: Insights from carbonate-hosted fault damage zones on the Maltese Islands. *Journal of Structural*
 987 *Geology*. 2017;101:43-57.

988 Drews MC, Hofstetter P, Zosseder K, Straubinger R, Gahr A, Stollhofen H. Predictability and
 989 controlling factors of overpressure in the North Alpine Foreland Basin, SE Germany: an
 990 interdisciplinary post-drill analysis of the Geretsried GEN-1 deep geothermal well. *Geothermal Energy*.
 991 2020;8(20):1-24. <https://doi.org/10.1186/s40517-020-00175-8>.

992 Du S. Prediction of permeability and its anisotropy of tight oil reservoir via precise pore-throat tortuosity
 993 characterization and “umbrella deconstruction” method. *Journal of Petroleum Science and Engineering*.
 994 2019;178:1018-28. <https://doi.org/10.1016/j.petrol.2019.03.009>

995 Eberli GP, Baechle GT, Anselmetti FS, Incze ML. Factors controlling elastic properties in carbonate
 996 sediments and rocks. *The Leading Edge*. 2003;22(7):654-60. <https://doi.org/10.1190/1.1599691>.

997 Fazlikhani H, Bauer W, Stollhofen H. Variscan structures and their control on latest to post-Variscan
 998 basin architecture: insights from the westernmost Bohemian Massif and SE Germany. *Solid Earth*.
 999 2022;13:393–416. <https://doi.org/10.5194/se-13-393-2022>.

1000 Fens TW. Petrophysical properties from small rock samples using image analysis techniques
 1001 [Dissertation]. TU Delft: Technical University Delft; 2000.

1002 Filomena CM, Stollhofen H. Ultrasonic logging across unconformities — outcrop and core logger sonic
 1003 patterns of the Early Triassic Middle Buntsandstein Hardegsen unconformity, southern Germany.
 1004 *Sedimentary Geology*. 2011;236(3-4):185-96.

1005 Freitag S, Drews M, Bauer W, Duschl F, Misch D, Stollhofen H. Cretaceous paleo-thicknesses in
 1006 Central Europe: New insights from shale compaction and thermal history analyses on the Franconian
 1007 Alb, SE Germany. *Solid Earth*. in review.

1008 Gao H, Li T, Yang L. Quantitative determination of pore and throat parameters in tight oil reservoir
 1009 using constant rate mercury intrusion technique. *Journal of Petroleum Exploration and Production*
 1010 *Technology*. 2016;6(2):309-18.

1011 Giesche H. Mercury Porosimetry: A general (practical) overview. *Particle & Particle Systems*
 1012 *Characterization*. 2006;23(1):9-19.

1013 Gosnold W, Lefever R, Mann M, Klenner R, McDonald M, Salehfar H. EGS potential in the northern
 1014 midcontinent of North America. *Geothermal Resources Council Transactions*. 2010;34:355-58.

1015 Graham B, Antonellini M, Aydin A. Formation and growth of normal faults in carbonates within a
 1016 compressive environment. *Geology*. 2003;31:11-14. [https://doi.org/10.1130/0091-](https://doi.org/10.1130/0091-7613(2003)031%3C0011:FAGONF%3E2.0.CO;2)
 1017 [7613\(2003\)031%3C0011:FAGONF%3E2.0.CO;2](https://doi.org/10.1130/0091-7613(2003)031%3C0011:FAGONF%3E2.0.CO;2).

1018 Gunter GW, Spain DR, Viro EJ, Thomas JB, Potter G, Williams J. Winland pore throat prediction
 1019 method - A proper retrospect: New examples from carbonates and complex systems. In: *SPWLA 55th*
 1020 *Annual Logging Symposium*, Abu Dhabi, United Arab Emirates, May 2014. 2014.

1021 Haines TJ, Michie EAH, Neilson JE, Healy D. Permeability evolution across carbonate hosted normal
 1022 fault zones. *Marine and Petroleum Geology*. 2016;72:62-82.

1023 Hall C, Hamilton A. Porosities of building limestones: using the solid density to assess data quality.
 1024 *Materials and Structures*. 2016;49(10):3969-79.

1025 Heap MJ, Baud P, Reuschlé T, Meredith PG. Stylolites in limestones: Barriers to fluid flow?. *Geology*.
 1026 2014;42(1):51-54.

1027 Hedtmann N, Alber M. Investigation of water-permeability and ultrasonic wave velocities of German
 1028 Malm aquifer rocks for hydro-geothermal energy. *Procedia Engineering*. 2017;191:127-33.

1029 Hofmann H, Weides S, Babadagli T, Zimmermann G, Moeck I, Majorowicz J, Unsworth M. Potential
 1030 for enhanced geothermal systems in Alberta, Canada. *Energy*. 2014;69:578-91.

1031 Homuth S, Götz AE, Sass I. Lithofacies and depth dependency of thermo- and petrophysical rock
 1032 parameters of the Upper Jurassic geothermal carbonate reservoirs of the Molasse Basin. *Zeitschrift der*

1033 Deutschen Gesellschaft für Geowissenschaften. 2014;165(3):469-86. <https://doi.org/10.1127/1860->
1034 1804/2014/0074.

1035 Homuth S, Götz AE, Sass I. Reservoir characterization of the Upper Jurassic geothermal target
1036 formations (Molasse Basin, Germany): role of thermofacies as exploration tool. *Geothermal Energy*
1037 *Science*. 2015;3(1):41-49. <https://doi.org/10.5194/gtes-3-41-2015>.

1038 Jennings JW, Lucia FJ. Predicting permeability from well logs in carbonates with a link to geology for
1039 interwell permeability mapping. *SPE Reservoir Evaluation & Engineering*. 2003;6(04):215-25.
1040 <https://doi.org/10.1016/j.enggeo.2020.105632>.

1041 Katz AJ, Thompson AH. Quantitative prediction of permeability in porous rock. *Physical Review B*.
1042 1986;34(11):8179-81.

1043 Katz AJ, Thompson AH. Prediction of rock electrical conductivity from mercury injection
1044 measurements. *Journal of Geophysical Research*. 1987;92(B1):599-607.

1045 Kiula U, McCarty DK, Derkowski A, Fischer TB, Prasad M. Total porosity measurement in gas shales
1046 by the water immersion porosimetry (WIP) method. *Fuel*. 2014;117:1115-29.
1047 <https://doi.org/10.1016/j.fuel.2013.09.073>.

1048 Klaver J, Desbois G, Urai JL, Littke R. BIB-SEM study of the pore space morphology in early mature
1049 Posidonia Shale from the Hils area, Germany. *International Journal of Coal Geology*. 2012;103:12-25.
1050 <https://doi.org/10.1016/j.coal.2012.06.012>.

1051 Klaver J, Hemes S, Houben M, Desbois G, Radi Z, Urai JL. The connectivity of pore space in
1052 mudstones: insights from high-pressure Wood's metal injection, BIB-SEM imaging, and mercury
1053 intrusion porosimetry. *Geofluids*. 2015;15(4):577-91. <https://doi.org/10.1111/gfl.12128>.

1054 Kley J, Voigt T. Late Cretaceous intraplate thrusting in central Europe: effect of Africa-Iberia-Europe
1055 convergence, not Alpine collision. *Geology*. 2008;36:839-42. <https://doi.org/10.1130/G24930A>.

1056 Klinkenberg LJ. The permeability of porous media to liquid and gases. *Drilling and production practice*.
1057 1941.

1058 Koch R, Weiss C. Field Trip A: Basin-Platform Transitions in Upper Jurassic Limestones and Dolomites
 1059 of the Northern Franconian Alb (Germany). *Zitteliana – An International Journal of Palaeontology and*
 1060 *Geobiology*. 2005;26:43-56.

1061 Köhler S, Duschl F, Fazlikhani H, Köhn D, Stephan T, Stollhofen H. Reconstruction of cyclic Mesozoic-
 1062 Cenozoic stress development in Southeastern Germany using fault-slip and stylolite inversion. *Geol.*
 1063 *Magazine*. in review.

1064 Koehn D, Rood MP, Beaudoin N, Chung P, Bons PD, Gomez-Rivas E. A new stylolite classification
 1065 scheme to estimate compaction and local permeability variations. *Sedimentary Geology*. 2016;346:60-
 1066 71. [https://doi.org/ 10.1016/j.sedgeo.2016.10.007](https://doi.org/10.1016/j.sedgeo.2016.10.007).

1067 Koepnick RB. Distribution and Permeability of Stylolite-Bearing Horizons Within a Lower Cretaceous
 1068 Carbonate Reservoir in the Middle East. *SPE Formation Evaluation*. 1987;2(02):137-42.

1069 Korneva I, Tondi E, Agosta F, Rustichelli A, Spina V, Bitonte R, Di Cuia R. Structural properties of
 1070 fractured and faulted Cretaceous platform carbonates, Murge Plateau (southern Italy). *Marine and*
 1071 *Petroleum Geology*. 2014;57:312-26. [https://doi.org/ 10.1016/j.marpetgeo.2014.05.004](https://doi.org/10.1016/j.marpetgeo.2014.05.004).

1072 Kozeny J. Über kapillare Leitung des Wassers im Boden: Sitzungsberichte der Wiener Akademie der
 1073 Wissenschaften. *Wiener Akademie der Wissenschaften*. 1927;136:271-306.

1074 Lala AMS, El-Sayed NAA. Controls of pore throat radius distribution on permeability. *Journal of*
 1075 *Petroleum Science and Engineering*. 2017;157:941-50.
 1076 <https://doi.org/10.1016/j.marpetgeo.2014.05.004>.

1077 Li Z, Wu S, Xia D, He S, Zhang X. An investigation into pore structure and petrophysical property in
 1078 tight sandstones: A case of the Yanchang Formation in the southern Ordos Basin, China. *Marine and*
 1079 *Petroleum Geology*. 2018;97:390-406. <https://doi.org/10.1016/j.marpetgeo.2018.07.014>.

1080 Lind IL, Berger WH, Kroenke LW, Mayer LA. Stylolites in chalk from leg 130, Ontong Java Plateau.
 1081 *Proceedings of the Ocean Drilling Program, scientific results*. 1993;130:445-51.

1082 Litsey LR, MacBride WL, Al-Hinai KM, Dismukes NB. Shuaiba Reservoir Geological Study, Yibal
 1083 Field, Oman. *Journal of Petroleum Technology*. 1986;38(06):651-61. [https://doi.org/ 10.2118/11454-](https://doi.org/10.2118/11454-PA)
 1084 PA.

1085 Lucia FJ. Rock-Fabric/Petrophysical Classification of Carbonate Pore Space for Reservoir
 1086 Characterization. *AAPG Bulletin*. 1995;79(9):1275-1300. [https://doi.org/10.1306/7834D4A4-1721-](https://doi.org/10.1306/7834D4A4-1721-11D7-8645000102C1865D)
 1087 11D7-8645000102C1865D.

1088 Lucia FJ. Permeability and Rock Fabric from Wireline Logs, Arab-D Reservoir, Ghawar Field, Saudi
 1089 Arabia. *GeoArabia*. 2001;6(4):619-46.

1090 Meyer RKF. Stratigraphie und Fazies des Frankendolomits (Malm) 2. Teil: Mittlere Frankenalb.
 1091 *Erlanger geologische Abhandlungen*. 1974;96:3-35.

1092 Micarelli L, Benedicto A, Invernizzi C, Saint-Bezar B, Michelot JL, Vergely P. Influence of P/T
 1093 conditions on the style of normal fault initiation and growth in limestones from the SE-Basin, France.
 1094 *Journal of Structural Geology*. 2005;27:1577-98. <https://doi.org/10.1016/j.jsg.2005.05.004>.

1095 Michie EAH. Influence of host lithofacies on fault rock variation in carbonate fault zones: A case study
 1096 from the Island of Malta. *Journal of Structural Geology*. 2015;76:61-79.
 1097 <https://dx.doi.org/10.1016/j.jsg.2015.04.005>.

1098 Mraz E. Reservoir characterization to improve exploration concepts of the Upper Jurassic in the
 1099 Southern Bavarian Molasse Basin [Dissertation]. TU München: Technical University of Munich; 2019.

1100 Mraz E, Bohnsack D, Stockinger G, Käsling H, Zosseder K, Thuro K. Die Bedeutung von
 1101 Analogaufschlüssen des Oberjura für die Interpretation der Lithologie der geothermalen Tiefbohrung
 1102 Geretsried. *Jahresberichte und Mitteilungen des Oberrheinischen Geologischen Vereins*. 2018;100:517-
 1103 47.

1104 Nenna F, Aydin A. The formation and growth of pressure solution seams in clastic rocks: A field and
 1105 analytical study. *Journal of Structural Geology*. 2011;33(4):633-43.
 1106 <https://doi.org/10.1016/j.jsg.2011.01.014>.

1107 Newsham KE, Rushing JA, Lasswell PM, Cox JC, Blasingame TA. A Comparative Study of Laboratory
 1108 Techniques for Measuring Capillary Pressures in Tight Gas Sands. In: SPE Annual Technical
 1109 Conference and Exhibition, Houston, Texas, U.S.A., 26-29 September 2004. 2004.
 1110 Nishiyama N, Yokoyama T. Estimation of permeability of sedimentary rocks by applying water-
 1111 expulsion porosimetry to Katz and Thompson model. *Engineering Geology*. 2014;177:75-82.
 1112 <https://doi.org/10.1306/070615142056>.
 1113 Okolo GN, Everson RC, Neomagus HWJP, Roberts MJ, Sakurovs R. *Fuel*. 2015;141:293-304.
 1114 <https://doi.org/10.1306/07061514205>.
 1115 O'Neill N. Fahud field review: A switch from water to gas injection. *Journal of Petroleum Technology*.
 1116 1988;40(05):609-18. <https://doi.org/10.1306/07061514205>.
 1117 Peterek A, Rauche H, Schröder B, Franzke H-J, Bankwitz P, Bankwitz E. The late- and post-Variscan
 1118 tectonic evolution of the Western Border fault zone of the Bohemian massif (WBZ). *Geologische*
 1119 *Rundschau*. 1997;86:191-202.
 1120 Pharaoh TC, Dusaar M, Geluk MC, Kockel F, Krawczyk CM, Krzywiec P, Scheck-Wenderoth M, Thybo
 1121 H, Vejbaek OV, Van Wees JD. Tectonic evolution. In: Doornenbal H, Stevenson AG, editors. *Petroleum*
 1122 *Geological Atlas of the Southern Permian Basin Area*, Utrecht: TNO Geological Survey of the
 1123 Netherlands; 2010. p. 25–57.
 1124 Philipp T, Amann-Hildenbrand A, Laurich B, Desbois G, Littke R, Urai JL. The effect of microstructural
 1125 heterogeneity on pore size distribution and permeability in Opalinus Clay (Mont Terri, Switzerland):
 1126 insights from an integrated study of laboratory fluid flow and pore morphology from BIB-SEM images.
 1127 *Geological Society, London, Special Publications*. 2017;454(1):85-106.
 1128 <https://doi.org/10.1144/SP454.3>.
 1129 Piénkowsk i G, Schudack ME, Bosák P, Enay R, Feldmann-Olszewska A, Golonka J, Gutowski J,
 1130 Herngreen GFW, Jordan P, Krobicki M, Lathuiliere B, Leinfelder RR, Michalík J, Mönnig E, Noe-
 1131 Nygaard N, Pálffy J, Pint A, Rasser MW, Reisdorf AG, Schmid DU, Schweigert G, Surlyk F, Wetzel A,

- 1132 Wong TE. Jurassic. In: McCann T. editor. The Geology of Central Europe. Volume 2: Mesozoic and
1133 Cenozoic. Bonn: The Geological Society London; 2008. p. 823-922.
- 1134 Rashid F, Glover PWJ, Lorinczi P, Hussein D, Collier R, Lawrence J. Permeability prediction in tight
1135 carbonate rocks using capillary pressure measurements. *Marine and Petroleum Geology*. 2015;68:536-
1136 50. <https://doi.org/10.1016/j.marpetgeo.2015.10.005>.
- 1137 Rashid F, Glover PWJ, Lorinczi P, Hussein D, Lawrence J. Microstructural controls on reservoir quality
1138 in tight oil carbonate reservoir rocks. *Journal of Petroleum Science and Engineering*. 2017;156:814-26.
1139 <https://doi.org/10.1016/j.petrol.2017.06.056>.
- 1140 Reicherter K, Froitzheim N, Jarosiński M, Badura J, Franzke H-J, Hansen M, Hübscher C, Müller R,
1141 Poprawa P, Reinecker J, Stackebrandt W, Voigt T, von Eynatten H, Zuchiewicz W. Alpine tectonics
1142 north of the Alps. In: McCann T. editor. The Geology of Central Europe. Volume 2: Mesozoic and
1143 Cenozoic. Bonn: The Geological Society London; 2008. p. 1233-86.
- 1144 Rustichelli A, Tondi E, Korneva I, Baud P, Vinciguerra S, Agosta F, Reuschlé T, Janiseck J-M. Bedding-
1145 parallel stylolites in shallow-water limestone successions of the Apulian Carbonate Platform (central-
1146 southern Italy). *Italian Journal of Geosciences*. 2015;134(3):513-34.
1147 <https://doi.org/10.3301/IJG.2014.35>.
- 1148 Sagi DA, De Paola N, McCaffrey KJW, Holdsworth RE. Fault and fracture patterns in low porosity
1149 chalk and their potential influence on sub-surface fluid flow – A case study from Flamborough Head,
1150 UK. *Tectonophysics*. 2016;690:35-51. <https://dx.doi.org/10.1016/j.tecto.2016.07.009>.
- 1151 Saki M, Siahpoush S, Khaz'ali AR. A new generalized equation for estimation of sandstone and
1152 carbonate permeability from mercury intrusion porosimetry data. 2020;10(7):2637-44.
1153 <https://doi.org/10.1007/s13202-020-00900-w>.
- 1154 Scheck-Wenderoth M, Krzywiec P, Zühlke R, Maystrenko Y, Froitzheim N. Permian to Cretaceous
1155 tectonics. In: McCann T. editor. The Geology of Central Europe. Volume 2: Mesozoic and Cenozoic.
1156 Bonn: The Geological Society London; 2008. p. 999-1030.

1157 Schröder B. Zur Morphogenese im Ostteil der Süddeutschen Scholle. *Geologische Rundschau*.
 1158 1968;58:10–32.

1159 Schröder B. Inversion tectonics along the western margin of the Bohemian Massif. *Tectonophysics*.
 1160 1987;137:93–100.

1161 Si L, Li Z, Yang Y. Influence of the Pore Geometry Structure on the Evolution of Gas Permeability.
 1162 *Transport in Porous Media*. 2018;123(2):321-39. <https://doi.org/10.1007/s11242-018-1044-z>.

1163 Sigal RF. A methodology for blank and conformance corrections for high pressure mercury porosimetry.
 1164 *Measurement Science and Technology*. 2009;20:1-11. <https://doi.org/10.1088/0957-0233/20/4/045108>.

1165 Sinn CJA, Klaver J, Fink R, Jiang M, Schmatz J, Littke R, Urai JL. *Geofluids*. 2017:1-19.
 1166 <https://doi.org/10.1155/2017/4709064>.

1167 Smodej J, Lemmens L, Reuning L, Hiller T, Klitzsch N, Claes S, Kukla PA. Nano- to Millimeter Scale
 1168 Morphology of Connected and Isolated Porosity in the Permo-Triassic Khuff Formation of Oman.
 1169 *Geosciences*. 2020;10(7):1-29. <https://doi.org/10.3390/geosciences10010007>.

1170 Tondi E. Nucleation, development and petrophysical properties of faults in carbonate grainstones:
 1171 Evidence from the San Vito Lo Capo peninsula (Sicily, Italy). *Journal of Structural Geology*.
 1172 2007;29:614-28. <https://doi.org/10.1016/j.jsg.2006.11.006>.

1173 Toussaint R, Aharonov E, Koehn D, Gratier J-P, Ebner M, Baud P, Rolland A, Renard F. Stylolites: A
 1174 review. *Journal of Structural Geology*. 2018;114:163-195. <https://doi.org/10.1016/j.jsg.2018.05.003>.

1175 Vejrbæk OV, Andersen C, Dusaar M, Herngreen GFW, Krabbe H, Leszczyński K, Lott GK, Mutterlose
 1176 J, Van der Molen AS. Cretaceous. In: Doornenbal H, Stevenson AG, editors. *Petroleum Geological*
 1177 *Atlas of the Southern Permian Basin Area*, Utrecht: TNO Geological Survey of the Netherlands; 2010.
 1178 p. 195-209.

1179 Voigt S, Aurag A, Leis F, Kaplan U. Late Cenomanian to Middle Turonian high-resolution carbon
 1180 isotope stratigraphy: New data from the Münsterland Cretaceous Basin, Germany. *Earth and Planetary*
 1181 *Science Letters*. 2007;253:196-210. <https://doi.org/10.1016/j.epsl.2006.10.026>.

1182 Voigt S, Wagreich M, Surlyk F, Walaszczyk I, Uličný D, Čech S, Voigt T, Wiese F, Wilmsen M,
 1183 Niebuhr B, Reich M, Funk H, Michalík J, Jagt JWM, Felder PJ, Schulp AS. Cretaceous. In: McCann
 1184 T. editor. The Geology of Central Europe. Volume 2: Mesozoic and Cenozoic. Bonn: The Geological
 1185 Society London; 2008. p. 923-98.

1186 Voigt T, Kley J, Voigt S. Dawn and dusk of Late Cretaceous basin inversion in central Europe'. Solid
 1187 Earth. 2021;12:1443–71. <https://doi.org/10.5194/se-12-1443-2021>.

1188 Von Eynatten H, Kley J, Dunkl I, Hoffmann V-E, Simon A. Late Cretaceous to Paleogene exhumation
 1189 in central Europe – localized inversion vs. large-scale domal uplift. Solid Earth. 2021;12:935–58.
 1190 <https://doi.org/10.5194/se-12-935-2021>.

1191 Wagner GA, Coyle DA, Duyster J, Henjes-Kunst F, Peterek A, Schröder B, Stöckhert B, Wemmer K,
 1192 Zulauf G, Ahrendt H, Bischoff R, Hejl E, Jacobs J, Menzel D, Lal N, van den Haute P, Vercoutere C,
 1193 Welzel B. Post-Variscan thermal and tectonic evolution of the KTB site and its surroundings. Journal
 1194 of Geophysical Research. 1997;102:18221–32.

1195 Washburn EW. The dynamics of capillary flow. Physical Review. 1921;17(3):273-83.

1196 Webb PA. An Introduction To The Physical Characterization of Materials by Mercury Intrusion
 1197 Porosimetry with Emphasis On Reduction And Presentation of Experimental Data. Micromeritics
 1198 Instruments Corp. 2001.

1199 Weger RJ, Baechle GT, Masaferro JL, Eberli GP. Effects of porestructure on sonic velocity in
 1200 carbonates. In: SEG 74th Annual Meeting, Dallas, Texas, U.S.A., 10-15 October 2004. 2004.
 1201 <https://library.seg.org/doi/10.1190/1.1845169>.

1202 Xu Y, Wang Y, Yuan H, Zhang D, Agostini F, Skoczylas F. Pore structure characterization of tight
 1203 sandstone from Sbaa Basin, Algeria: Investigations using multiple fluid invasion methods. Journal of
 1204 Natural Gas Science and Engineering. 2018;59:414-26. <https://doi.org/10.1016/j.jngse.2018.09.021>.

1205 Zeiss A. Jurassic Stratigraphy of Franconia. Stuttgarter Beiträge zur Naturkunde. Serie B. 1977;31:1-
 1206 32.

- 1207 Zeybeck M, Kuchuk FJ. Fault and fracture characterization using 3D interval pressure transient tests.
1208 In: Abu Dhabi International Petroleum Exhibition and Conference. Abu Dhabi, United Arab
1209 Emirates, 13-16 October 2002. 2002.
- 1210 Zhao X, Yang Z, Lin W, Xiong S, Wei Y. Characteristics of microscopic pore-throat structure of tight
1211 oil reservoirs in Sichuan Basin measured by rate-controlled mercury injection. *Open Physics*.
1212 2018;16(1):675-84. <https://doi.org/10.1515/phys-2018-0086>.
- 1213 Ziauddin ME, Bize E. The effect of pore scale heterogeneities on carbonate stimulation treatments. In:
1214 SPE Middle East Oil and Gas Show and Conference, Manama, Bahrain, March 11-14 2007.
- 1215 Ziegler PA. Geological Atlas of Western and Central Europe (2nd edition). Geological Society
1216 Publishing House. 1990.
- 1217 Ziegler PA, Cloetingh S, van Wees JD. Dynamics of intraplate compressional deformation: the Alpine
1218 foreland and other examples. *Tectonophysics*. 1995;252:7-59.
- 1219 Zinszner B, Pellerin F-M. A geoscientist's guide to petrophysics. Paris: Editions Technip; 2007.

1220 **11. Appendix**

1221

1222

1223

Table A- 1: For determining the best permeability estimation model, the mean residual square error (MRSE) in relation to the corresponding permeabilities measured with air and argon and standard deviation (σ) for each model and used porosity method (Archimedes porosity (Arch), He-pycnometry (He); MICP (Hg)) were calculated.

Model	Arch-Porosity						He-Porosity						Hg-Porosity						Overall	
	Air			Ar			Air			Ar			Air			Ar			Rank	
	MRSE	σ	Rank	MRSE	σ	Rank	MRSE	σ	Rank	MRSE	σ	Rank	MRSE	σ	Rank	MRSE	σ	Rank	Air	Ar
K-T-Model	0.15	0.15	2	0.23	0.26	3	0.13	0.11	1	0.33	0.18	3	0.19	0.18	2	0.20	0.29	3	1	3
Winland-Model	0.36	0.33	4	0.20	0.15	2	0.65	0.44	4	0.42	0.27	4	0.28	0.33	4	0.20	0.16	3	4	3
Dastidar-Model	0.56	0.23	6	0.26	0.14	4	0.89	0.33	6	0.58	0.30	6	0.55	0.36	6	0.35	0.34	4	6	5
K-C-Model	0.44	0.70	5	0.92	1.53	7	0.23	0.25	3	0.32	0.51	2	0.42	0.40	5	0.53	0.73	6	5	6
Bohnsack-Model	0.13	0.21	1	0.29	0.41	5	0.78	0.44	5	0.44	0.28	5	0.21	0.19	3	0.14	0.23	2	3	4
GPPT-Model	0.72	0.32	7	0.30	0.17	6	1.26	0.58	7	0.73	0.20	7	0.69	0.41	7	0.40	0.19	5	7	7
Saki-Model	0.17	0.10	3	0.03	0.02	1	0.20	0.12	2	0.04	0.03	1	0.17	0.11	1	0.03	0.02	1	2	1
No porosity used																				
Capillary-tube-Model	Air						Ar													
	$\tau = 2.00$			$\tau = 1.57$			$\tau = 2.00$			$\tau = 1.57$										
	MRSE		σ		MRSE		σ		MRSE		σ		MRSE		σ		MRSE		σ	
	0.06		0.06		0.17		0.14		0.05		0.03		0.00		0.00					

1224